Mean-Field Theory of Collective Behavior of Quantum Dipolar Rotors

by

Bo Liu

A thesis
presented to the University of Waterloo
in fulfillment of the
thesis requirement for the degree of
Master of Science
in
Physics

Waterloo, Ontario, Canada, 2020

Author's Declaration

I hereby declare that I am the sole author of this thesis. This is a true copy of the thesis, including any required final revisions, as accepted by my examiners.

I understand that my thesis may be made electronically available to the public.

Statement of Contributions

The content of the Chapter 3 of this thesis is the outcome of a collaboration with Dr. Jeff Rau, who provided supervision together with my supervisor Michel Gingras. The content of the Chapter 4 Sec. 4.1 is the outcome of a collaboration with Addison Richards and Ying Luo for discussing and checking the Ewald summation results and Luttinger-Tisza eigenvalues. Yulia Kalugina provided the screened dipole moment for molecules confined in C_{60} computed using *ab initio* method.

Abstract

Motivated by the recent experimental measurements of the dielectric property of confined quantum dipolar molecules, the orientational dipolar ordering transition is investigated in the quantum generalization of the quantum dipole rotor model. As a result of the competition between dipole-dipole interaction and rotational kinetic energy, the confined quantum dipolar molecule is predicted to have a quantum phase transition from a disordered phase (paraelectric) to an ordered phase, which depends on the lattice structure if the dipole-dipole interaction is sufficiently strong. The quantum phase transitions of dipoles confined to the vertices of face-centered cubic (FCC) lattices and triangular lattice is studied using mean-field theory. We first study the ground state configuration using the iterative minimization method and Luttinger-Tisza method. Then, the phase diagram, as a function of the dipolar interaction's strength, is constructed. The study shows the orientational phases of quantum dipolar rotors whose properties are determined by the strength of the dipole-dipole interaction, the rotational constant, and the dipolar molecule's shape. An interesting phenomenon called reentrance is found for some symmetric and asymmetric molecules.

Acknowledgements

First and foremost, I would like to express my sincere appreciation to my supervisor, Prof. Michel Gingras. Thank you for providing priceless guidance in research and life, especially being patient helping me polish the manuscript of the C_{60} paper. Thank you for having made everything possible to do this thesis.

I would like to extend my gratitude to my examining committee; Prof. Pierre-Nicholas Roy and Prof. Kazi Rajibul Islam for their help and feedback to enhance this thesis. I would like to thank Dr. Jeff Rau for your patient guidance in the C_{60} project. I would also like to thank Dr. Wen Jin for your help and discussion in polishing the manuscript of the C_{60} paper. Also, Addison Richards and Ying Luo for discussing and checking the results of the Ewald summation code. I would like to extend my thanks to Jianying Sheng, Aritro Mukherjee, Cyrus Xu Cerkauskas, Kristian Tyn-Kai Chung, Daniel Lozano Gomez, Darren Pereira for much help and conversations during my program.

I wish to express my sincere gratitude to all my friends and my family for their encouragement.

Dedication

This is dedicated to people I love.

Table of Contents

List of Tables

List of Figures

Chapter 1

Introduction

Confined polar molecules have drawn great attention because they provide a fascinating platform to explore collective phenomena that emerge from the complicated interactions between the microscopic degrees of freedom associated with the constituents of a system and quantum phase transition that appears due to quantum fluctuations. It has recently become possible to embed polar molecules, e.g., HF and H_2O in the interior of C_{60} molecules [2, 3, 4], which was predicted as ferroelectric materials [5]. Moreover, Dressel's group recently found that confined water molecules in beryl and cordierite exhibit a tendency towards a macroscopic alignment of their [2, 3, 4] dipoles [6, 7]. In this work, the quantum phase transition and collective behavior for the above systems are studied. To address the collective behavior of polar molecules and investigate quantum phase transitions with confined quantum dipolar molecules, a review of the endofullerene and confined water molecule in beryl and cordierite is first provided. Finally, the fundamental research motivation and objective of this work and the outline of this thesis are given.

1.1 Confined quantum molecules

1.1.1 Buckminsterfullerene and endohedral fullerenes

A fullerene is a family allotrope of carbon that consists of carbon atoms connected by single and double bonds that form a closed or partially closed mesh. The molecule may be a hollow sphere, ellipsoid, tube, or many other shapes and sizes. One of the most famous fullerene members is Buckminsterfullerene, also known as buckyball or soccer ball, and

was discovered in 1985 [8]. With a chemical formula of C_{60}, Buckminsterfullerene has a cage-like fused-ring structure made of twenty hexagons, and twelve pentagons of the carbon atoms share 90 covalent bonds between them [9]. The pentagon is made of 5 electron-poor single bonds, and the hexagon is made of 3 single bonds and 3 double bonds, and there are 30 electron-rich double bonds and 60 electron-poor single bonds in total in the C_{60}. In the

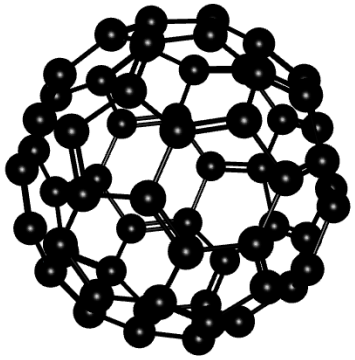

Figure 1.1: Molecular structure of the C_{60}. Buckminsterfullerene has a hollow sphere shape, and the cavity is large enough for encapsulating small molecules.

solid state, C_{60} molecules crystallizes into face centred cubic (FCC) lattice structure with the lattice constant $a_0 = 14.17$ Å and the nearest-neighbour distance is 10.02 Å at room temperature and ambient pressure [10]. The C_{60} molecules are located at the lattice points of an FCC lattice. The FCC phase of C_{60} undergoes a phase transition to a simple cubic (SC) phase with the space group $Pa\bar{3}$ at characteristic temperature $T_c = 257(1)$ K [10] due to rotational freezing of the individual C_{60} cages and the lattice constant a_0 decreases slightly.

The structure and cavity inside C_{60} make it possible to encapsulate a single molecule inside and provides a unique environment to study the isolated atoms and molecules. A guest atom or molecule is trapped in the interior of a host molecule is called endohedral compounds. Fullerenes with additional atoms, ions or clusters enclosed within their inner spheres are so-called endohedral fullerenes or endofullerenes. Lanthanum atom was the first atom to be trapped inside a carbon cage, and the endohedral compound is denoted as La@C_{60} [11]. The notation of the molecule encapsulated within a buckyball is usually written as X@C_{60}. X is the guest atom or molecule, and all atoms listed on the right of the @ symbol are assumed to be part of the cage [11]. The endofullerene was synthesized by a procedure called molecular surgery [2, 3, 4]. Molecular surgery is a technique, which involves a series of chemical reactions to open a hole on the cage of a size suitable to

allow encapsulation of the single guest molecule, then insert the guest molecule into the hole, and close the hole. The detailed procedures to synthesize $H_2@C_{60}$ and $H_2O@C_{60}$ was pioneered by Komatsu [2] and Murata [2, 12]. Procedures for the synthesis of $HF@C_{60}$ [13] and $CH_4@C_{60}$ [4] then reported by Whitby's group. The reasons that motivated people to synthesize endofullerene are the need to storage molecules and drug delivery [14, 15].

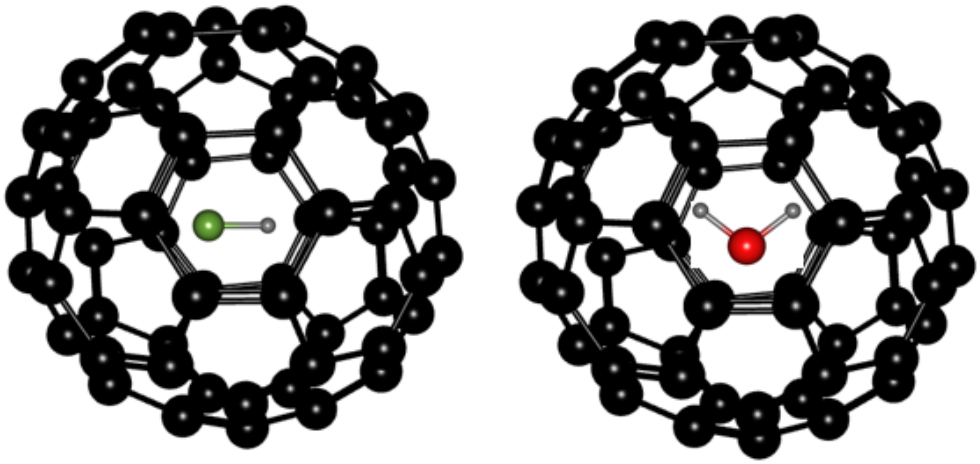

(a) $HF@C_{60}$ (b) $H_2O@C_{60}$

Figure 1.2: The demonstration of the endofullerene. The approximately spherical 3.7 Å diameter cavity provides a unique environment in which to isolate a single molecule.

The fascinating endofullerene system is rich in quantum phenomena and provides one of the most promising platforms for exploring quantum phase transition driven by dipole-dipole interaction. The electric dipole lattices of C_{60} with an encapsulated polar molecule were theoretically predicted to have ferroelectricity due to the dipolar interaction by Cioslowski and Nanayakkara [5]. They estimated the transition temperature of the dipolar lattice T_0 using $T_0 = \alpha T^*$ from the dimensional analysis, where α is a constant and $T^* = \mu^2(k_b a_0^3)^{-1}$. T^* is called characteristic temperature, μ is the screened dipole moment at each lattice site (a counter dipole moment on the C_{60} cage induced by encapsulation of the polar water molecule can reduce the total dipole moment), and k_b is Boltzmann's constant. $H_2O@C_{60}$ crystal was predicted to have a ferroelectric phase transition below 64 K by using $T_0 = \alpha T^*$ [3].

In order to reveal the fundamental properties and the interesting quantum phenomena of water molecules in the non-hydrogen bonding environments, the endofullerene $H_2O@C_{60}$

has been extensively studied [13, 16], e.g., ortho-para spin conversion, rotational level-splitting, and long-range dipole correlations. Aoyagi's group measured dielectric permittivities of both $H_2O@C_{60}$ and C_{60} against temperature [3]. The dielectric permittivity of the empty fullerene remains relatively constant as temperature decreases. However, the dielectric permittivity of $H_2O@C_{60}$ endohedral fullerene increases with decreasing temperature. In Fig. 3a of Aoyagi's paper [3], it can be seen the dielectric permittivity diverge at about 8 K. This shows that the dielectric permittivity or electrical susceptibility of the $H_2O@C_{60}$ single-crystal follows the Curie–Weiss law, and the Curie temperature T_C is equal to 8 K. The permittivity measurement suggests that the crystal may exhibit a ferroelectric phase transition below 8 K and under high pressure.

1.1.2 Water in beryl and cordierite

Beryl is a mineral found mainly in pegmatitic rocks, composed of beryllium aluminium cyclosilicate with the chemical formula $Be_3Al_2Si_6O_{18}$ (Fig. 1.3, panel (d)). The crystal structure contains channels of 5.1 Å in diameter which consists of six-membered rings of SiO_4 tetrahedra linked by AlO_6 octahedra and BeO_4 tetrahedra along c-axis (Fig. 1.3, panel (a)). The channel has a cavity in the middle which is large enough for trapping a single water molecule. There are also impurity alkali ions that exist in beryl, e.g., Cs, Rb, K, Na, which lies in the bottleneck (Fig. 1.3, panel (b)). The presence of impurity ions is due to a charge imbalance in the framework because of the isomorphic substitution of Al and Be(which form cages) by lower valency cations (Al^{3+} to Mg^{2+}, $Fe^{2+/3+}$, Mn^{2+}, Cr^{3+}, Vr^{3+}, and Be^{2+} to Li^{+}) [18, 19]. In this work, we do not consider the effect of impurity ions.

A single-crystal neutron diffraction study of an alkali/water-rich beryl and an alkali/water-poor beryl performed by Artioli *et al.* [18] shows that there are two types of water on the basis of the presence of impurity ions. In beryl with a high content of alkali ion, the H_2O's dipole moment and H···H vectors point along c-axis (Water II). In alkali-poor beryl, the strong H_2O electric dipole is oriented within the ab-plane (Water I)(Fig. 1.3, panel (b)) [17, 19]. Some experimental and theoretical studies, based on spectroscopic, terahertz–infrared (3–7000 cm^{-1}) spectra [17], neutron scattering experiments investigations, and ab initio charge density analysis [6, 20, 21, 22, 23], provided some new insights into the alkali-poor beryl, such as quantum tunneling of H_2O protons and collective behavior of H_2O. For H_2O molecules in beryl, a ferroelectric soft mode, whose frequency is going down as the temperature is approaching the T_C (the phonon "softens") becoming zero at T_C (T_C is Curie temperature), was observed. In the Ref. [6], the temperature evolution of dielectric permittivity of a beryl crystal was measured (see Figure 3 in Ref. [6]), and

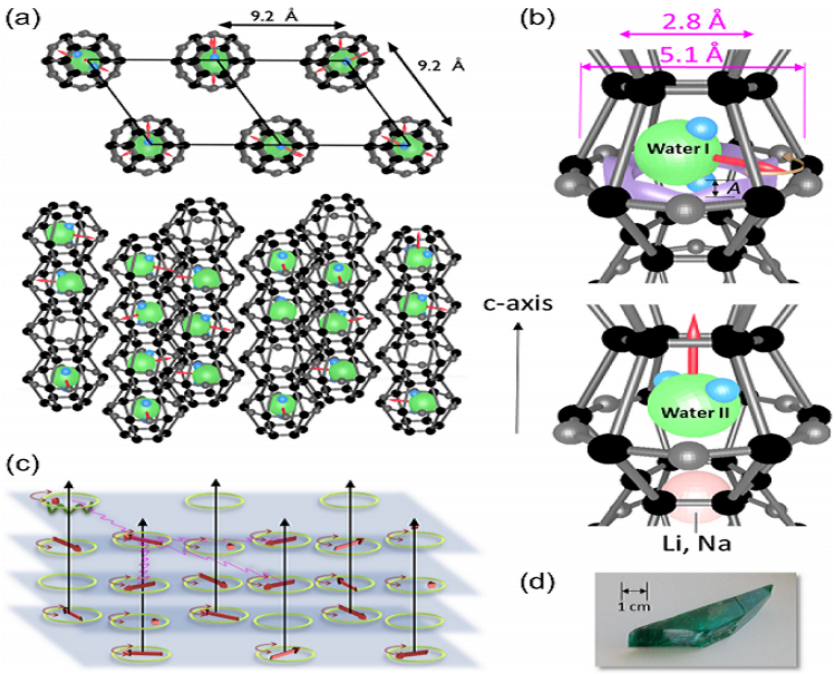

Figure 1.3: Schematic view of water molecules in nano-sized cages of the beryl crystal lattice. (a) H_2O molecules confined in the channels within the beryl crystal lattice. Three-dimensional and top views with the crystal plotted dark gray and the water molecules colored (oxygen green and hydrogen blue). The one-dimensional channels are arranged in a hexagonal fashion with 9.2 Å distance and contain cages in a distance of 4.6 Å. (b) Water molecules located within structural voids formed by lattice ions. The cages (diameter 5.1 Å) are separated by narrower bottlenecks (2.8 Å). Molecules of type I have their dipole moments (red arrows) perpendicular to the crystallographic c-axis with the plane of H_2O molecules parallel to c; they can perform hindered rotations around the c-axis experiencing a six-well potential (depth A) due to the hexagonal crystal symmetry. Type-II water molecules are turned by 90° relative to those of type I due to Coulomb interactions with alkali ions (Li and Na, shown in yellow) blocking the bottleneck; their dipole moments are directed along the c-axis. (c) Dipole moments of type-I molecules. The moments can rotate within the planes perpendicular to the c-axis. The dipole–dipole interactions (magenta wavy lines) act between the molecular dipoles within the channels where molecular doublets, triplets, and so on are formed; the interactions between dipoles in adjacent channels are much weaker owing to their greater mutual distances. (d) Photograph of the typical studied beryl crystal. Reprinted (adapted) with permission from (J Infrared Milli Terahz Waves (2018) 39:799–815). Copyright (2018) American Chemical Society [17].

the dielectric permittivity followed the Curie–Weiss law. The frequency of the soft mode is shown in Figure 5 in Ref. [6] which follows the Cochran law. These results suggest that H_2O molecules in beryl exhibit the tendency towards a ferroelectric order.

Similar to beryl (see Fig. 1.4), cordierite is also an interesting example to study the collective behavior of confined water molecules. Cordierite is a mineral composed of magnesium iron aluminum cyclosilicate with the chemical formula $(Mg, Fe)_2Al_4Si_5O_{18}$. Similar to beryl, which contains Si_6O_{18} rings, two of six silicon atoms in cordierite are replaced by aluminum, leading to $(Si, Al)_6O_{18}$ rings that are stacked along the c-axis and form channels with a cavity. The lattice exhibits orthorhombic symmetry space group $Cccm53$. Recently, the collective behavior of water molecules is studied experimentally and theoretically [7]. The dielectric permittivity measurement, *ab* initio molecular dynamics and classical Monte Carlo simulations presented in Ref. [7] suggest a ferroelectric phase in the ab-plane and antiferroelectrically order along the channel direction.

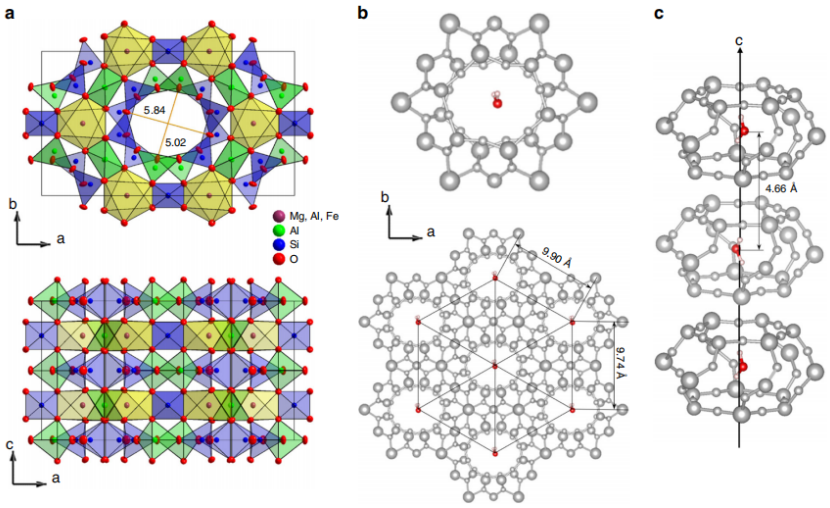

Figure 1.4: Cordierite crystal structure with water molecules within ionic nanopores. **a** Unit cell of cordierite crystal from X-ray analysis with thermal ellipsoids at 85 K. **b** The water molecules within cordierite nanopores form two-dimensional triangular lattice within the ab-plane. **c** One-dimensional chain of confined water molecules along the c-axis. Reprinted (adapted) with permission from Creative Commons Attribution 4.0 International License (https://creativecommons.org/licenses/by/4.0/). The source is from Ref. [7]. No changes were made.

1.2 Background information for quantum rotor

To help the reader understand the model we will discuss later, we briefly introduce the background information for the quantum rotor.

In general, the rotational motion of a rigid rotor is characterized by three principal moments of inertia I_a, I_b and I_c, and $I_a < I_b < I_c$ [24]. The Hamiltonian for the rotational motion of a rigid body can be written as

$$\begin{aligned} H_{\text{Rotation}} &= \frac{\mathbf{J}_a^2}{2I_a} + \frac{\mathbf{J}_b^2}{2I_b} + \frac{\mathbf{J}_c^2}{2I_c} \\ &= A\mathbf{J}_a^2 + B\mathbf{J}_b^2 + C\mathbf{J}_c^2, \end{aligned} \tag{1.1}$$

where $A \geq B \geq C$ are rotational constants of three principle axis, $\mathbf{J}_a$, $\mathbf{J}_b$ and $\mathbf{J}_c$ are angular momentum components in body-fixed frame (principle axis system). Molecules as rigid rotor are grouped into four classes based on their three principal moments shown in Table. 1.1. For example, HF is a linear molecule, NH_3 is an oblate symmetric top molecule, CCl_4 is a spherical top molecule and CH_2Cl_2 is an asymmetric top molecule.

linear	$I_a = 0,\ I_b = I_c$
symmetric top	$I_a < I_b = I_c$
spherical top	$I_a = I_b = I_c$
asymmetric top	$I_a < I_b < I_c$

Table 1.1: Classification of rigid rotors

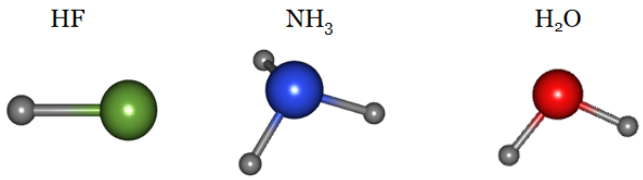

Figure 1.5: The demonstration of the rigid rotor class. HF is a linear molecule, NH_3 is a symmetric molecule, and H_2O is an asymmetric molecule.

1.3 The collective behavior and quantum phase transition driven by dipole interaction

Having shown the background information of the endofullerene and confined water molecule in beryl and cordierite, we next introduce and discuss the collective behavior and quantum phase transition driven by dipole interaction. Quantum phase transitions are driven by quantum fluctuations between different ground states at the absolute zero temperature. The quantum phase transition we are interested in is the order-disorder transition, where a quantum critical point separates the ordered phase and disordered phase. In this section, the quantum phase transition for the dipolar rotor system is introduced.

Polar molecules possessing a permanent electric dipole moment interact at long range via the anisotropic dipole-dipole interaction potential

$$V_{ij} = \frac{1}{4\pi\epsilon_0} \frac{\mathbf{d}_i \cdot \mathbf{d}_j - 3(\mathbf{d}_i \cdot \hat{\mathbf{r}}_{ij})(\mathbf{d}_j \cdot \hat{\mathbf{r}}_{ij})}{|\mathbf{r}_{ij}^3|}, \tag{1.2}$$

where $\mathbf{d}_i$ is the electric dipole moment of the i^{th} molecule and the relative position $\mathbf{r_{ij}} = \mathbf{r}_i - \mathbf{r}_j$ between the two polar molecules at sites i and j. Then the simplest model, quntum rotor model with dipole-dipole interaction, to describe the confined dipolar rotors can be written as

$$H = \sum^{N} \frac{\mathbf{J}^2}{2I} + \sum_{j>i} V_{ij}, \tag{1.3}$$

where I is the moment of inertia and $\mathbf{J}$ is the angular momentum operator.

The first part of the Eq. (1.3) is formed by the rotational eigenstates, e.g., $|JM\rangle$ for the linear rotor, and $|JKM\rangle$ for symmetric rotor and asymmetric rotor cases (see Appendix B for details). The kinetic energy is minimized when the orientation of the rotor is maximally uncertain according to the uncertainty principle. Hence, the first term in Eq. (1.3) prefers a disordered state (paraelectric) in which the rotors do not exhibit a specific orientation, i.e., $\langle \mathbf{p} \rangle = 0$, where $\mathbf{p}$ denotes the polarization. This can be shown by parity argument or performed in position space using integrals over the spherical harmonics [25], i.e.,

$$\begin{aligned}
\langle p_z \rangle &= d \int |Y_{J'}^{M'}(\theta, \phi)|^2 \cos\theta \; d\Omega = 0, \\
\langle p_x \rangle &= d \int |Y_{J'}^{M'}(\theta, \phi)|^2 \sin\theta \cos\phi \; d\Omega = 0, \\
\langle p_y \rangle &= d \int |Y_{J'}^{M'}(\theta, \phi)|^2 \sin\theta \sin\phi \; d\Omega = 0.
\end{aligned} \tag{1.4}$$

The second part of the Eq. (1.3) is anisotropic long-range interaction energy, which is minimized by some ordered configuration with non-zero polarization, i.e., $\langle \mathbf{p} \rangle \neq 0$. Lattinger and Tisza found that the ground state of freely rotating dipoles of face centered cubic (FCC) or body centered cubic (BCC) lattice is ordered ferroelectrically [26], while the simple cubic lattice of dipoles has an anti-ferroelectric ground state [27].

In summary, the dipole-dipole potential makes the system favor an ordered state, while the rotational part of the Hamiltonian of the system makes the system favor a disordered state. As a result of the competition between the potential and kinetic energies, there is a quantum critical point at zero temperature. Therefore, as the strength of the dipole-dipole interaction increases, the rotational symmetry may be broken, and a quantum phase transition from a paraelectric phase to a ferroelectric phase occurs. The goal of this project is to understand the collective behavior and the order-disorder phase transition driven by dipole interaction. We aim to search for potential ferroelectric materials theoretically to suggest chemists a direction to synthesize the potential ferroelectric materials we found.

1.4 Outline of the thesis

In this thesis, the goal is to study the quantum dipolar rotors' collective behavior and construct the order-disorder phase diagrams (which will be introduced later) for the linear rotor, symmetric top rotor, and asymmetric top rotor. In the introduction of this thesis, the background information of several confined quantum molecules, quantum phase transition of the quantum dipole rotor model, is given, aiming to give the reader a general understanding of the order-disorder phase transition for the confined dipolar molecules. The remaining part of this work consists of four chapters. Chapter 2 introduces the quantum dipole rotor model and the mean-field approximation to accomplish our objective. To simplify the mean-field Hamiltonian, one needs to know the ground state configuration of the classical dipoles. Hence, the iterative minimization method and Luttinger-Tisza method are introduced to find the ground state configuration. Chapter 3 and Chapter 4 report the results for FCC lattice and triangular lattice. Chapter 5 shows the application of our results. In Chapter 6, we conclude this work with a summary and an outlook of our work.

Chapter 2

Methods

2.1 Mean-field approximation for confined quantum dipolar rotor

Only few of the many-body system models can be solved exactly. Even the simplest case, the Ising model, is not solved exactly in dimensionality higher than two. The renormalization group technique is powerful but difficult in practical calculations for each problem of quantum many-body systems. Hence, the mean-field approximation is often the first method chosen to study critical phenomena and the mean-field study allows a semi-quantitative exploration of the phase transition. Another method that can be used is the Monte Carlo method, a recent study of the dipoles confined to the vertices of two-dimensional lattices obtained by the quantum mo the order-disorder phase diagram by the Monte Carlo method [28]. In Ref. [28], they only consider the linear type rotor.

In this work, we use mean-field theory to study the orientational order-disorder phase transition for the linear, symmetric, and asymmetric rotor. In this Chapter, a detailed construction of the mean-field approximation is given.

2.1.1 Mean-field approximation for quantum dipole rotor model

In general, the energy for the confined quantum dipolar rotor can be written as

$$H = H_{\text{Rotor}} + H_{\text{Dipole}} + H_{\text{Crystal}}, \tag{2.1}$$

where H_{Rotor} is the rotational kinetic energy of the confined molecules, H_{Dipole} is the dipole-dipole interaction, H_{Crystal} is the crystal field due to the cage's effect from confinement. In this work, we mainly focus on the competition between H_{Rotor} and H_{Dipole} to reveal a general understanding of the order-disorder phase transition. To study the collective behavior of confined quantum dipolar rotor and investigate how the anisotropic dipole-dipole interaction breaks the symmetry of the rotational Hamiltonian, we first start by describing the mean-field approximation of the dipole-dipole interaction.

To describe the interaction between the dipolar molecules whose dipole moments $\mathbf{d}$ are along the z-axis of their body-fixed frame, we sum over all pairs of site i and j in Eq. (1.2)

$$\begin{aligned} H_{\text{Dipole}} &= \sum_{i>j} \frac{1}{4\pi\epsilon_0}\left(\frac{\mathbf{d}_i \cdot \mathbf{d}_j - 3(\mathbf{d}_i \cdot \hat{\mathbf{r}}_{ij})(\mathbf{d}_j \cdot \hat{\mathbf{r}}_{ij})}{|\mathbf{r}_{ij}^3|}\right), \\ &= D \sum_{i>j} \frac{\hat{\mathbf{n}}_i \cdot \hat{\mathbf{n}}_j - 3(\hat{\mathbf{n}}_i \cdot \hat{\mathbf{r}}_{ij})(\hat{\mathbf{n}}_j \cdot \hat{\mathbf{r}}_{ij})}{|\mathbf{r}_{ij}^3|}, \\ &= D \sum_{i>j} \Lambda_{ij}^{\alpha\beta} n_i^\alpha n_j^\beta, \end{aligned} \tag{2.2}$$

where $D \equiv \frac{d^2}{4\pi\epsilon_0}$, $\Lambda_{ij}^{\alpha\beta} \equiv \frac{\delta^{\alpha\beta} r^2 - 3 r_{ij}^\alpha r_{ij}^\beta}{|\mathbf{r}_{ij}^5|}$, and $\alpha, \beta = X, Y, Z$ in the lab frame. The many-body Hamiltonian for confined quantum dipolar rotors system can be written as

$$H = H_{\text{Rotor}} + D \sum_{i>j} \Lambda_{ij}^{\alpha\beta} n_i^\alpha n_j^\beta. \tag{2.3}$$

The rotational kinetic energy is characterized by the rotational constants and competes with the dipole-dipole interaction. However, the dipole-dipole interaction favors the breaking of symmetry, and the strength of the interaction depends on the interaction matrix $\Lambda_{ij}^{\alpha\beta}$, which is characteristic of the lattice structure, and the dipole moment, i.e., the magnitude of D. Next, we write n_i^α in Eq. (2.3) as

$$n_i^\alpha = n_i^\alpha + \langle n_i^\alpha \rangle - \langle n_i^\alpha \rangle, \tag{2.4}$$

where $\langle n_i^\alpha \rangle = \frac{1}{Z} \text{Tr}\left[n_i^\alpha \exp\{-\beta H_{\text{MF}}\}\right]$. $\beta = \frac{1}{k_B T}$, k_B is the Boltzmann constant, and $Z = \text{Tr} \exp\{-\beta H_{\text{MF}}\}$ is the partition function. Therefore,

$$\begin{aligned} n_i^\alpha n_j^\beta &= (n_i^\alpha + \langle n_i^\alpha \rangle - \langle n_i^\alpha \rangle) \cdot (n_j^\beta + \langle n_j^\beta \rangle - \langle n_j^\beta \rangle), \\ &= (n_i^\alpha - \langle n_i^\alpha \rangle) \cdot (n_j^\beta - \langle n_j^\beta \rangle) + n_i^\alpha \cdot \langle n_j^\beta \rangle + n_j^\beta \cdot \langle n_i^\alpha \rangle - \langle n_j^\beta \rangle \cdot \langle n_j^\beta \rangle. \end{aligned} \tag{2.5}$$

The mean-field approximation assumes the fluctuations of the polarization from their expectation value are small, i.e., $(n_i^\alpha - \langle n_i^\alpha \rangle) \cdot (n_j^\beta - \langle n_j^\beta \rangle) = 0$ in Eq. (2.5). Ignoring the fluctuations, the mean-field Hamiltonian Eq. (2.3) can be written as

$$H_{\mathrm{MF}} = H_{\mathrm{Rotor}} + D \sum_{i>j} \Lambda_{ij}^{\alpha\beta} (\langle n_i^\alpha \rangle n_j^\beta + n_i^\alpha \langle n_j^\beta \rangle - \langle n_i^\alpha \rangle \langle n_j^\beta \rangle). \tag{2.6}$$

Equation (2.6) is the general expression for the site-dependent mean-field Hamiltonian for a dipolar rotor system. Applying the mean-field approximation, the many interacting dipolar rotors problem is converted into a single dipolar rotor in an effective electric field problem. In the following sections, we show how to solve the mean-field self-consistent equation numerically, derive the free energy using perturbation theory, and calculate the susceptibility to fully understand the confined quantum dipolar rotor's collective behavior and construct the orientational order-disorder phase diagram.

2.1.2 Free energy and self-consistent equation

Having the mean-field Hamiltonian Eq. (2.6), we define the on-site polarization as the order parameter, i.e., $p = \langle \hat{n} \rangle$ and the partition function as

$$Z = \mathrm{Tr}\, \exp\{-\beta H_{\mathrm{MF}}\}, \tag{2.7}$$

Then we can derive free energy of the system as

$$F = -k_{\mathrm{B}} T \ln Z. \tag{2.8}$$

Minimizing the free energy, one obtains the exact expression of self-consistent equation $p = \langle \hat{n} \rangle$. Combining the appropriate matrix elements and numerically exact diagonalizations, p can be solved in a self-consistent manner. We use an iteration method to solve $p = \langle \hat{n} \rangle$. Start with an arbitrary small p, plug it into the right hand side of $p = \langle \hat{n} \rangle$ and obtain a new p'. After obtaining a converged value for p, we then stop the iteration procedure.

2.2 Configuration of classical dipolar rotor

The general mean-field construction for the confined dipolar rotor system is given in the previous section. Equation (2.6) is the most general expression for the site-dependent mean-field Hamiltonian for a dipolar rotor system. As mentioned earlier, the dipoles favor

some specifically ordered orientations, at which the free energy is minimized. After knowing the ordered orientations favored by the dipole-dipole interaction, one can simplify Eq. (2.6) and solve the whole problem.

In this section, two methods to find and interpret the ground state configuration of dipoles are described. The first method for finding the ground state configuration is the iterative minimization method. It is an iterative computational method that can find the ground states of a finite set of spins on a lattice with some given boundary conditions. The second method is Luttinger-Tisza method [26, 29] which is a theoretical method to determine the ordering wavevectors or momentums. The ordering wavevectors are the wavevectors at which the dipolar system minimizes its energy. Once we find the ordering wavevectors, comparing the ordering wavevectors to the iterative minimization simulation helps determine whether the simulation has found the true ground state configuration.

2.2.1 Iterative minimization method

The iterative minimization method is a method that searches the ground state configuration by lowering the energy of a system of dipoles initially pointing in random directions iteratively. From Eq. (2.2), the local or on-site electric field of site i can be written as

$$\mathbf{E}_i = -D \sum_j \Lambda_{ij} \mathbf{n}_j. \tag{2.9}$$

The idea is that the interaction energy of a set of dipoles initially pointing in random directions can be minimized by reorienting the dipoles so that they point along their local electric field's direction. The iterative procedure works in the following way. We start with the N dipoles on the lattice pointing in random directions. Next, we run a large loop for an unspecified number of iterations. On each iteration of the loop, N dipoles are reoriented to point along their electric field's direction. The loop stops when the difference between the energy of new set($(i+1)^{th}$ loop) of dipole vectors and the old set(i^{th} loop) is smaller than some specified value ϵ ($\epsilon = 10^{-5}$ in our calculations), i.e.

$$|E_{i+1} - E_i| < \epsilon, \tag{2.10}$$

and the final configuration is the ground state configuration favored by dipole-dipole interaction.

This procedure does not always find the true ground state configuration, because the dipoles sometimes can be trapped in some local minima with pretty close energy to the true ground state configuration.

2.2.2 Luttinger-Tisza method

Luttinger-Tisza (LT) method [26, 29] is a technic that minimizes the energy of the system of spins by Fourier transform the dipole-dipole interaction and find the specific wavevector $\mathbf{q}$ in the Brillouin zone at which a system of dipoles has the lowest energy. In general, the Hamiltonian of interacting spins on a Bravais lattice can be written as

$$H = \frac{1}{2}\sum_{i\neq j} J_{ij}\mathbf{s}_i \cdot \mathbf{s}_j, \tag{2.11}$$

where all the dipoles are normalized $|s_i|^2 = 1$, and it is called the 'strong constraint'. We want to find a set of $\mathbf{s}_i$ which minimizes Eq. (2.11) for a given J_{ij}. This problem is hard to solve by using the 'strong constraint'. The 'strong constraint' implies $\sum_i^N |s_i|^2 = N$, and it is called the 'week constraint'. The idea is that we can solve the problem with the 'week constraint' and check if the solution satisfies the 'strong constraint'. By using the week constraint, we have the Lagrange multiplier

$$H = \frac{1}{2}\sum_{i\neq j} J_{ij}\mathbf{s}_i \cdot \mathbf{s}_j - \lambda(\sum_i |s_i|^2 - N). \tag{2.12}$$

The problem becomes to minimize [29]

$$\sum_j J_{ij}\mathbf{s}_j = \lambda \mathbf{s}_i. \tag{2.13}$$

First, we write $\mathbf{s}_i$ as a sum of Fourier modes

$$\mathbf{s}_i = \frac{1}{\sqrt{N}}\sum_{\mathbf{q}} \tilde{\mathbf{s}}(\mathbf{q}) e^{i\mathbf{q}\cdot\mathbf{r}_i}. \tag{2.14}$$

Then, Eq. (2.11) can be written as

$$\begin{aligned} H &= \frac{1}{2}\sum_{i\neq j} J_{ij}(\frac{1}{\sqrt{N}}\sum_{\mathbf{q}} \tilde{\mathbf{s}}(\mathbf{q}) e^{i\mathbf{q}\cdot\mathbf{r}_i}) \cdot \frac{1}{\sqrt{N}}\sum_{\mathbf{q}'} \tilde{\mathbf{s}}'(\mathbf{q}') e^{i\mathbf{q}'\cdot\mathbf{r}_j}, \\ &= \frac{1}{2N}\sum_{i\neq j}\sum_{q,q'} J_{ij}\mathbf{s}(\mathbf{q}) \cdot \tilde{\mathbf{s}}(\mathbf{q}') e^{i(\mathbf{q}+\mathbf{q}')\cdot\mathbf{r}_i} \cdot e^{-i\mathbf{q}'\cdot\mathbf{r}_{ij}}, \end{aligned} \tag{2.15}$$

where $\mathbf{r}_{ij} = \mathbf{r}_i - \mathbf{r}_j$. Using the orthogonality relations for discrete Fourier transforms

$$\frac{1}{N}\sum_i e^{i(\mathbf{q}+\mathbf{q}')\cdot\mathbf{r}_i} = \delta_{-\mathbf{q},\mathbf{q}'}, \tag{2.16}$$

Eq. (2.15) can be written as

$$H = \frac{1}{2}\sum_{j}\sum_{q} J_{ij}\ \mathbf{s}(\mathbf{q})\cdot\tilde{\mathbf{s}}(-\mathbf{q})e^{i\mathbf{q}\cdot\mathbf{r}_{ij}}. \tag{2.17}$$

Next, we define the quantity $\tilde{J}(\mathbf{q})$, the Fourier transform of the coupling J_{ij} between site i and j, to be

$$\tilde{J}(\mathbf{q}) = \frac{1}{2}\sum_{j} J_{ij}e^{i\mathbf{q}\cdot\mathbf{r}_{ij}}. \tag{2.18}$$

So we can write Hamiltonian as

$$\begin{aligned} H &= \sum_{\mathbf{q}} \tilde{J}(\mathbf{q})\mathbf{s}(\mathbf{q})\cdot\tilde{\mathbf{s}}(-\mathbf{q}), \\ &= \sum_{\mathbf{q}} \tilde{J}(\mathbf{q})|\mathbf{s}(\mathbf{q})|^2. \end{aligned} \tag{2.19}$$

In order to minimize Hamiltonian, we need to choose the wavevector $\mathbf{q}^*$ which minimizes the lowest eigenvalue of $\tilde{J}(\mathbf{q})$. Once we find the wavevector $\mathbf{q}^*$, the total energy of the system can be written as

$$H = N\tilde{J}(\mathbf{q}^*), \tag{2.20}$$

since $\sum_{\mathbf{q}}|\mathbf{s}(\mathbf{q})|^2 = N$, if the spins are normalized. We may write out the final form of the ground state as a coplanar spiral involving only the wavevector $\mathbf{q}^*$ [29]

$$\mathbf{s_i} = \cos(\mathbf{q}^*\cdot\mathbf{r_i}+\phi)\hat{\mathbf{A}} + \sin(\mathbf{q}^*\cdot\mathbf{r_i}+\phi)\hat{\mathbf{B}}, \tag{2.21}$$

where ϕ is a phase factor, and $\hat{\mathbf{A}}$ and $\hat{\mathbf{B}}$ are the unit vectors in the real space, i.e. X,Y,Z. In general, Eq. (2.20) is true only if the solution does not conflict with the 'strong constraint'. The LT method yields an (often rather useful) guess at possible ground states and a lower bound $N\tilde{J}(\mathbf{q}^*)$ on the energy.

2.3 Summary

In this chapter, the mean-field approximation and two methods to search the ordered configuration of dipoles for different lattice structure were discussed. The mean-field approximation is used in Chapter 3 and 4, and obtains a general mean-field Hamiltonian. We

then used the iterative minimization method and Luttinger-Tisza method [26, 29] to search the ordered configuration of dipoles and simplified the mean-field Hamiltonian according to the ordered configuration of dipoles. In the following two chapters, the orientational order-disorder phase transition of quantum dipolar rotors for FCC and triangular lattice is studied by the mean-field method.

Chapter 3

Mean-field study of confined dipolar molecule in Buckminsterfullerene

As introduced in Sec. 1.1, fullerenes have been intensively studied. The diameter of C_{60} is 0.7 nm, so the interior of the fullerenes can be viewed as a container [15]. It provides a platform to study the confined quantum molecules and their collective behavior. Especially, some of the guest molecules that can be trapped in C_{60} are dipolar molecules, e.g., HF and H_2O [3, 30]. The trapped molecules can rotate and translate almost freely within C_{60} cages [31], but some of the degenerated energy levels are split due to the C_{60} cage's effect [32, 33]. C_{60} forms an FCC lattice at room temperature and ambient pressure, and has a structural phase transitions to SC lattice as temperature decreases to 257 K [10]. In this work, we simply treat the C_{60} as an FCC lattice, and the confined dipoles are on the FCC lattice sites. We also ignore the translational motion of the trapped molecules and C_{60} cage's potential acting on the trapped molecules. Then, the endofullerenes lattice can be described by

$$H = H_{\text{Rotor}} + H_{\text{Dipole}}. \tag{3.1}$$

Because of the different energy level structures of different types of rotors, i.e., linear, symmetric, and asymmetric rotor, the phase diagrams have distinct features. In the above equation, the Hamiltonian is characterized by the molecules' dipole moment, lattice structure, and rotational constants. Once we know this information, we can solve the orientational ordering problem.

3.1 Mean-field Hamiltonian of the FCC lattice

Following the procedure introduced in Sec. 2.1.1, we write

$$H = \sum_i \left(A\mathbf{J}_a^2 + B\mathbf{J}_b^2 + C\mathbf{J}_c^2\right) + D\sum_{i>j} \Lambda_{ij}^{\alpha\beta} n_i^\alpha n_j^\beta, \tag{3.2}$$

where $D \equiv \frac{d^2}{4\pi\epsilon_0}$, $\Lambda_{ij}^{\alpha\beta} \equiv \frac{\delta^{\alpha\beta}r^2 - 3r_{ij}^\alpha r_{ij}^\beta}{|\mathbf{r}_{ij}^5|}$, and $\alpha, \beta = X, Y, Z$ in the lab frame. Then we apply mean-field approximation

$$H_{\mathrm{MF}} = \sum_i (A\mathbf{J}_a^2 + B\mathbf{J}_b^2 + C\mathbf{J}_c^2) + D\sum_{i>j} \Lambda_{ij}^{\alpha\beta}(\langle n_i^\alpha\rangle n_j^\beta + n_i^\alpha\langle n_j^\beta\rangle - \langle n_i^\alpha\rangle\langle n_j^\beta\rangle), \tag{3.3}$$

where $\langle n_i^\alpha\rangle = \frac{1}{Z}\mathrm{Tr}\left[n_i^\alpha \exp\{-\beta H_{\mathrm{MF}}\}\right]$. As the dipoles for the FCC lattice have a ferroelectric ground state [26], we first assume the average polarization as order parameter along Z-direction in lab frame, i.e. $p_i \equiv \langle n_i^Z\rangle = \langle\cos\theta_i\rangle$ when the dipole-dipole interaction is significantly strong. This way,

$$H_{\mathrm{MF}} = \sum_i^N \left[A\mathbf{J}_a^2 + B\mathbf{J}_b^2 + C\mathbf{J}_c^2 + \frac{1}{2}D\sum_j \Lambda_{ij}^{ZZ}(p_i\cos\theta_j + p_j\cos\theta_i - p_ip_j)\right], \tag{3.4}$$

where Λ_{ij}^{ZZ} is the ZZ component of the $\Lambda_{ij}^{\alpha\beta}$ matrix. If the system has uniform ferroelectric order, we can drop the index lable of the $p_i = \langle\cos\theta_i\rangle$ and Eq. (3.4) simplifies to

$$H_{\mathrm{MF}} = \sum_i^N \left[A\mathbf{J}_a^2 + B\mathbf{J}_b^2 + C\mathbf{J}_c^2 - \lambda_i(p\cos\theta - \frac{1}{2}p^2)\right], \tag{3.5}$$

where we have defined the dipolar lattice sum $\lambda_i \equiv -D\sum_j \Lambda_{ij}^{ZZ}$ (the index label of λ_i can also be dropped and we drop it henceforth). Actually, $-\lambda p\cos\theta$ is the energy of the single dipole in an electric field generated from all other dipoles. Thus, we convert a many interacting dipolar rotors problem to a single dipolar rotor in an effective electric field problem, and Eq. (3.5) is in fact a Stark effect Hamiltonian with a constant energy shift. The single rotor Hamiltonian is

$$H_i = \left[A\mathbf{J}_a^2 + B\mathbf{J}_b^2 + C\mathbf{J}_c^2 - \lambda_i(p\cos\theta - \frac{1}{2}p^2)\right]. \tag{3.6}$$

3.1.1 Local mean-field equations and iterative solutions

The partition function of the Eq. (3.5) is

$$\begin{aligned} Z &= \mathrm{Tr}\, \exp\{-\beta H_{\mathrm{MF}}\}, \\ &= C \prod_{i}^{N} \mathrm{Tr}[\exp\{-\beta(A\mathbf{J}_a^2 + B\mathbf{J}_b^2 + C\mathbf{J}_c^2 - \lambda p \cos\theta\}], \end{aligned} \tag{3.7}$$

where $C = \exp\{-\frac{1}{2}\beta\lambda p^2\}$. Then, we have the expression of the free energy. Because of the difficulty to obtain the analytical expression of the trace in Eq. (3.7), we derive the expression of the self-consistent equation by the definition of the polarization rather than from minimizing the free energy. By the definition $p = \langle \cos\theta \rangle$, and combining the appropriate matrix elements and numerically exact diagonalizations of Eq. (3.6), we have

$$\begin{aligned} p &= \langle \cos\theta \rangle\,, \\ &= \frac{\sum_n \langle \phi_n | \cos\theta | \phi_n \rangle\, e^{-\beta E_n}}{\sum_n e^{-\beta E_n}}, \end{aligned} \tag{3.8}$$

where E_n and $|\phi_n\rangle$, as functions of p, are the energy and wave function of the n-th state of a single rotor. We use an iteration method to solve Eq. (3.8). We start with an arbitrary small p , plug it into the right hand side of Eq. (3.8) and obtain a new p'. We then have so obtained the right hand side of Eq. (3.8) again and again, until one obtains a converged value for p.

Working out the single-site solution, we can also iterate the self-consistent equation site-dependently for every dipolar rotor

$$\begin{aligned} \mathbf{p}_i &= \frac{\mathbf{E}_i}{|\mathbf{E}_i|} \langle \cos\theta_i \rangle\,, \\ &= \frac{\mathbf{E}_i}{|\mathbf{E}_i|} \frac{\sum_n \langle \phi_{in} | \cos\theta_i | \phi_{in} \rangle\, e^{-\beta E_{in}}}{Z_i}, \end{aligned} \tag{3.9}$$

for the magnitude of the polarization vector and calculate the on-site electric field to capture the direction. The idea is to first initialize the system by giving each lattice site a small random polarization vector $\mathbf{p}_i$. Then, one uses Ewald method [34] (Appendix A) to calculate the dipolar lattice sum λ_i for a site i and so obtained local on-site electric field $\mathbf{E}_i$ and use Eq. (3.9) to calculate the magnitude of the polarization vector. The local polarization is updated "in place", which means that once a new polarization vector for a single site is calculated, it replaces the old polarization vector and is instantaneously used in the subsequent calculation for the other sites in a cubic simulation box of length L with periodic boundary conditions [35, 36].

3.1.2 Free energy calculation

Assuming a uniform ferroelectric phase ($\mathbf{p}_i = p\hat{z}$ for all sites), the partition function of Eq. (3.8) can be written in the form

$$\begin{aligned} Z &= \prod_i^N \mathrm{Tr}\big[\exp\{-\beta(H_{\mathrm{Rotation}} + H_{\mathrm{Dipole}})\}\big], \\ &= \prod_i^N \sum_n \exp\Big\{-\beta(\frac{1}{2}\lambda p^2 + E_n^{(0)} + E_n^{(1)} + E_n^{(2)} + E_n^{(3)} + E_n^{(4)})\Big\}, \end{aligned} \tag{3.10}$$

where $E_n^{(0)}$ are the energies of the unperturbed rotational states [24], $E_n^{(1)}$, $E_n^{(2)}$, $E_n^{(3)}$ and $E_n^{(4)}$ are the corresponding first, second, third and fourth order corrections [37] due to the perturbation H_{Dipole} treated in the mean-field approximation. Hence, we can derive the free energy

$$F = -k_{\mathrm{B}}T \ln Z, \tag{3.11}$$

where $\exp\Big\{-\beta(E_n^{(1)} + E_n^{(2)} + E_n^{(3)} + E_n^{(4)})\Big\}$ can be expanded using $e^x = 1 + x + \frac{x^2}{2} + ...$

$$\begin{aligned} \frac{F}{N} \cong \frac{1}{2}\lambda p^2 - k_{\mathrm{B}}T \ln \sum_n \exp\big\{-\beta E_n^{(0)}\big\} 1 - \beta E_n^{(1)} + \frac{1}{2}\beta^2 (E_n^{(1)})^2 - \beta E_n^{(2)} + \beta^2 E_n^{(1)} E_n^{(2)} \\ - \beta E_n^{(3)} + \frac{1}{2}\beta^2 (E_n^{(2)})^2 - \beta E_n^{(4)} + \beta^2 E_n^{(1)} E_n^{(3)}. \end{aligned} \tag{3.12}$$

We define the Z_n functions as

$$\begin{aligned} Z_0 = \sum_n z_n^0, \quad Z_1 = \sum_n z_n^0 \beta \frac{E_n^{(1)}}{\lambda p}, \quad Z_2 = \sum_n \frac{1}{2} z_n^0 \beta^2 \frac{(E_n^{(1)})^2}{(\lambda p)^2}, \quad Z_3 = \sum_n z_n^0 \beta \frac{E_n^{(2)}}{(\lambda p)^2}, \\ Z_4 = \sum_n z_n^0 \beta^2 \frac{E_n^{(1)} E_n^{(2)}}{(\lambda p)^3}, \quad Z_5 = \sum_n z_n^0 \beta \frac{E_n^{(3)}}{(\lambda p)^3}, \quad Z_6 = \sum_n \frac{1}{2} z_n^0 \beta^2 \frac{(E_n^{(2)})^2}{(\lambda p)^4}, \\ Z_7 = \sum_n z_n^0 \beta \frac{E_n^{(4)}}{(\lambda p)^4}, \quad Z_8 = \sum_n z_n^0 \beta^2 \frac{E_n^{(1)} E_n^{(3)}}{(\lambda p)^4}, \end{aligned} \tag{3.13}$$

with $z_n^0 \equiv \exp\Big\{-\beta E_n^{(0)}\Big\}$. Even though rigid rotor eigenstates with the same quantum number J are degenerate, the non-degenerate perturbation theory can still be used to calculate $E_n^{(1)}$, $E_n^{(2)}$, $E_n^{(3)}$ and $E_n^{(4)}$. The reason is that the dipole interaction as a perturbation

does not connect states of the same energy. The expression of the perturbation energy is given [37] as

$$
\begin{aligned}
E_n^{(1)} &= V_{nn}, \\
E_n^{(2)} &= -\sum_{j\neq n} \frac{V_{nj}V_{jn}}{D_{jn}}, \\
E_n^{(3)} &= \sum_{jk\neq n} \frac{V_{nj}V_{jk}V_{kn}}{D_{jn}D_{kn}} - V_{nn}\sum_{j\neq n}\frac{V_{nj}V_{jn}}{D_{jn}^2}, \\
E_n^{(4)} &= [\sum_{i\neq n}\frac{V_{ni}V_{in}}{D_{jn}}][\sum_{j\neq n}\frac{V_{nj}V_{jn}}{D_{jn}^2}] - V_{nn}^2\sum_{j\neq n}\frac{V_{nj}V_{jn}}{D_{jn}^3} \\
&\quad + V_{nn}\sum_{ij\neq n}[\frac{1}{D_{in}^2 D_{jn}} + \frac{1}{D_{in}D_{jn}^2}]V_{ni}V_{ij}V_{jn} \\
&\quad - \sum_{ijk\neq n}\frac{1}{D_{in}D_{jn}D_{kn}}V_{ni}V_{ij}V_{jk}V_{kn},
\end{aligned}
\tag{3.14}
$$

where $V_{ij} = \langle i|H_{\text{Dipole}}|j\rangle$ in our case and $D_{ij} = E_i - E_j$ is the difference of the energy between rotational state i and state j. Equation (3.12) then becomes

$$
\begin{aligned}
\frac{F}{N} &= \lambda p^2 - k_{\text{B}}T\ln\,[Z_0 - Z_1\lambda p + (Z_2 - Z_3)(\lambda p)^2 + (Z_4 - Z_5)(\lambda p)^3 + (Z_6 - Z_7 + Z_8)(\lambda p)^4], \\
&= -k_{\text{B}}T\ln Z_0 + [\frac{1}{2}\lambda - k_{\text{B}}T\lambda^2\frac{Z_2 - Z_3}{Z_0}]p^2 + k_{\text{B}}T\lambda^4[\frac{1}{2}(\frac{Z_2 - Z_3}{Z_0})^2 - \frac{Z_6 - Z_7 + Z_8}{Z_0}]p^4.
\end{aligned}
\tag{3.15}
$$

We expanded the logarithm and collected all terms in the same order in p. All odd power terms in p vanish for all types of rotors, which implies the ferroelectric state has no preference of any specific direction. The p^4 term in Eq. (3.15) is always positive by calculating the Z_n functions and the p^2 term changes sign at a critical temperature T_c which shows the phase transition is of second order. According to the Ginzburg-Landau theory of second-order phase transition, the critical temperature T_c can be solved at a given λ by finding where the coefficient of the quadratic term in Eq. (3.15) changes sign, i.e., solving

$$
\frac{1}{2}\lambda - k_{\text{B}}T\lambda^2(\frac{Z_2 - Z_3}{Z_0}) = 0. \tag{3.16}
$$

The critical temperature and the corresponding λ gives the phase boundary between the paraelectric and ferroelectric phases.

3.1.3 Electric susceptibility calculation

The electric susceptibility measures how much a material will become polarized in an applied electric field. A tiny external field could induce a net polarization of the system at the paraelectric to ferroelectric phase boundary, so the electric susceptibility diverges at the phase boundary. Assume an external electric field $\mathbf{h} = h\hat{z}$, which helps the dipolar system to select a particular direction in which to align, is added. Eq. (3.5) becomes

$$H_{\mathrm{MF}} = \sum_{i}^{N} \left[A\mathbf{J}_a^2 + B\mathbf{J}_b^2 + C\mathbf{J}_c^2 - \lambda(p\cos\theta - \frac{1}{2}p^2) - h\cos\theta \right], \tag{3.17}$$

Following the similar steps as those leading to Eq. (3.15), we calculate the free energy in presence an external electric field

$$\frac{F}{N} = -k_{\mathrm{B}}T \ln Z_0 + \frac{1}{2}\lambda p^2 - k_{\mathrm{B}}T(\frac{Z_2 - Z_3}{Z_0})(\lambda p + h)^2, \tag{3.18}$$

where we dropped the higher order terms in p, because p a phase boundary is small and higher order terms are not important. Minimizing F with respect to h, we obtain

$$\begin{aligned} p &= \frac{2k_{\mathrm{B}}T(\frac{Z_2-Z_3}{Z_0})h}{1 - 2k_{\mathrm{B}}T(\frac{Z_2-Z_3}{Z_0})\lambda}, \\ &\equiv \frac{\chi^0 h}{1 - \lambda\chi^0}, \end{aligned} \tag{3.19}$$

where we have defined the quantity χ^0 as

$$\chi^0 = 2k_{\mathrm{B}}T(\frac{Z_2 - Z_3}{Z_0}). \tag{3.20}$$

We thus obtain the electric susceptibility as

$$\chi = \frac{\partial p}{\partial h}|_{h=0} = \frac{\chi^0}{1 - \lambda\chi^0}, \tag{3.21}$$

which has a Curie-Weiss form [38]. At a second order phase boundary, the electric susceptibility diverges, giving

$$1 - \lambda\chi^0 = 0. \tag{3.22}$$

Following the Ref. [38], it can be shown that χ_0 is the non-interacting electric susceptibility of a single rotor, and we can derive the electric susceptibility Eq. (3.21) in another way. If the effective external electric field is changed by a small amount δh along the z-axis, then the energy for the n-th state becomes $E_n^{(1)} = E_n^{(0)} - \langle\phi_n|\cos\theta\,|\phi_n\rangle\,\delta h$ using first order perturbation theory, and the corresponding eigenstate is

$$\left|\phi_n^{(1)}\right\rangle = |\phi_n\rangle - \delta h \sum_{n'} \frac{|\phi_{n'}\rangle\,\langle\phi_{n'}|\cos\theta\,|\phi_n\rangle}{(E_n^{(0)} - E_{n'}^{(0)})}. \tag{3.23}$$

Hence

$$\begin{aligned}
\langle\cos\theta\rangle &= \sum_n \left\langle\phi_n^{(1)}\right|\cos\theta\left|\phi_n^{(1)}\right\rangle \exp\left\{-\beta E_n^{(1)}\right\}/Z, \\
&= \sum_n \langle\phi_n|\cos\theta\,|\phi_n\rangle \exp\left\{-\beta E_n^{(1)}\right\}/Z \\
&\quad - 2\,\delta h \sum_{nn'} \langle\phi_n|\cos\theta\,|\phi_{n'}\rangle\,\langle\phi_{n'}|\cos\theta\,|\phi_n\rangle \exp\left\{-\beta E_n^{(1)}\right\}/Z,
\end{aligned} \tag{3.24}$$

where $Z = \sum_n \exp\left\{-\beta E_n^{(0)}\right\}$ is the single molecule partition function. We take derivative of above equation with respect to δh to calculate non-interacting susceptibility

$$\begin{aligned}
\chi^0 &= \frac{\partial\,\langle\cos\theta\rangle}{\partial\ \delta h}, \\
&= -2 \sum_{nn'}^{E_n^{(0)}\neq E_{n'}^{(0)}} \frac{\langle\phi_n|\cos\theta\,|\phi_{n'}\rangle\,\langle\phi_{n'}|\cos\theta\,|\phi_n\rangle}{E_n^{(0)} - E_{n'}^{(0)}} \exp\left\{-\beta E_n^{(0)}\right\}/Z \\
&\quad + \beta \sum_{nn'}^{E_n^{(0)}=E_{n'}^{(0)}} \langle\phi_n|\cos\theta\,|\phi_{n'}\rangle\,\langle\phi_{n'}|\cos\theta\,|\phi_n\rangle \exp\left\{-\beta E_n^{(0)}\right\}/Z \\
&\quad - \beta\,\langle\cos\theta\rangle^2 \\
&= \frac{2}{\beta}\left(\frac{-Z_3}{Z_0} + \frac{Z_2}{Z_0}\right) - \beta\,\langle\cos\theta\rangle^2,
\end{aligned} \tag{3.25}$$

where Z_2 and Z_3 are defined in Eq. (3.13). Because the average polarization $p \equiv \langle\cos\theta_i\rangle = 0$ in the paraelectric phase, we drop the last term. Now, we have re-derived χ^0 using perturbation method. By the definition of the susceptibility $\chi = \frac{\chi^0}{1-\lambda\chi^0}$ [38], we recover Eq. (3.21).

3.2 Exact diagnalization

In this section, the basis set functions for different rotor types and the details of writing the dipole-dipole interaction under mean-field approximation are introduced. The goal of the section is to find the eigenvectors and eigenvalues of the mean-filed Hamiltonian.

3.2.1 Linear rotor

For a linear molecule, the moment of inertia about the principal axis a is zero and the two other moments of inertia along axes b and c are I i.e. $I_a = 0$ and $I_b = I_c$. It requires the angular moment of axis a to be zero to prevent Eq. (1.1) from going to infinity. The rotational motion of a linear molecule can thus be written as

$$H_{\text{Rotation}}^{\text{linear}} = \frac{\mathbf{J_b}^2}{2I} + \frac{\mathbf{J_c}^2}{2I} = B\mathbf{J}^2, \tag{3.26}$$

where we identification of axis $a \leftrightarrow z$, $b \leftrightarrow x$ and $c \leftrightarrow y$[1]. As angular momentum is perpendicular to the a-axis or z-axis in the body-fixed frame, i.e. $K = 0$, the symmetric top wave function $|J0M\rangle$ is reduces to the spherical harmonic wave function $|JM\rangle$, i.e., $Y_{JM}(\theta, \phi) = (\frac{2J+1}{4\pi})^{\frac{1}{2}} D^{J*}_{M0}(\theta, \phi, \chi)$. $|JM\rangle$ is the basis set functions that diagonalize $\mathbf{J^2}$ and J_Z

$$\begin{aligned} \left\langle J'M' \middle| \mathbf{J}^2 \middle| JM \right\rangle &= J(J+1)\delta_{J'J}\delta_{M'M} \\ \left\langle J'M' \middle| \mathbf{J}_Z \middle| JM \right\rangle &= M\delta_{J'J}\delta_{M'M}. \end{aligned} \tag{3.27}$$

So the energy for each energy level only depends on quntum number J and is given by

$$E(J, M) = J(J+1)B. \tag{3.28}$$

Having the matrix elements for the rotational kinetic energy, we then show how to write the dipole-dipole interaction under mean-field approximation, i.e., $\cos\theta$ in the $|JM\rangle$ basis. The matrix elements of $\cos\theta$ can be written in term of integrals over products of spherical

[1] In this thesis, capital letter X, Y, Z represent the space-fixed frame axis and small letter x, y, z or a, b, c represent the body-fixed frame.

harmonics

$$\begin{aligned}\langle J'M'|\cos\theta|JM\rangle &= \iint [Y_{J'}^{M'}(\theta,\phi)]^* \cos\theta\, Y_J^M(\theta,\phi)\, d\theta\, d\phi \\ &= \sqrt{\frac{4\pi}{3}} \iint [Y_{J'}^{M'}(\theta,\phi)]^* Y_1^0(\theta,\phi) Y_J^M(\theta,\phi)\, d\theta\, d\phi \\ &= \sqrt{\frac{(2J+1)}{(2J'+1)}}\, \langle J0;10|J'0\rangle\, \langle JM;10|J'M'\rangle\,, \end{aligned} \tag{3.29}$$

where $\langle J0;10|J'0\rangle$ and $\langle JM;10|J'M'\rangle$ are Clebsch-Gordan coefficients. To calculate Eq. (3.29), one can use Table 2.4 frequently used Clebsch-Gordan coefficients in Ref. [24] . Finally, Eq. (3.29) reads

$$\langle J'M'|\cos\theta|JM\rangle = \begin{cases} \sqrt{\frac{(J-M+1)(J+M+1)}{(2J+3)(2J+1)}} & \text{if} \quad J'=J+1 \quad \text{and} \quad M'=M, \\ \sqrt{\frac{(J-M)(J+M)}{(2J-1)(2J+1)}} & \text{if} \quad J'=J-1 \quad \text{and} \quad M'=M. \end{cases} \tag{3.30}$$

The dipole selection rules for the linear rotor which can be seen from Eq. (3.29) are $M = M'$ and $J' = J \pm 1$. The dipole selection rules imply that the non-degenerate perturbation theory works in dipole-dipole interaction calculations because the dipole operator only connects two states with a different energy.

3.2.2 Symmetric top rotor and asymmetric top rotor

There are two classes of the symmetric top rotor, i.e., oblate symmetric top (disk shape) rotor and prolate symmetric top (cigar shape) rotor.

In the oblate top limit $I_a = I_b < I_c$ and we identification of axis $a \leftrightarrow x$, $b \leftrightarrow y$ and $c \leftrightarrow z$. The identification of the axis helps us simplify Eq. (1.1)

$$\begin{aligned} H_{\text{Rotation}}^{\text{symmetric}} &= \frac{\mathbf{J}_a^2}{2I_a} + \frac{\mathbf{J}_b^2}{2I_a} + \frac{\mathbf{J}_c^2}{2I_c}, \\ &= A\mathbf{J}_a^2 + B\mathbf{J}_b^2 + C\mathbf{J}_c^2, \\ &= A\mathbf{J}^2 + (C-A)\mathbf{J}_z^2. \end{aligned} \tag{3.31}$$

As $A = B$, we can rewrite the second line to the third line in Eq. (3.31). The energies are

$$E(J,M) = AJ(J+1) + (C-A)K^2. \tag{3.32}$$

In the prolate top limit $I_a < I_b = I_c$, Eq. (1.1) becomes

$$\begin{aligned} H_{\text{Rotation}}^{\text{symmetric}} &= \frac{\mathbf{J}_a^2}{2I_a} + \frac{\mathbf{J}_b^2}{2I_a} + \frac{\mathbf{J}_c^2}{2I_c}, \\ &= A\mathbf{J}_a^2 + B\mathbf{J}_b^2 + C\mathbf{J}_c^2, \\ &= C\mathbf{J}^2 + (A-C)\mathbf{J}_z^2, \end{aligned} \tag{3.33}$$

where we redefine the body-fixed coordinates $a \leftrightarrow z$, $b \leftrightarrow x$ and $c \leftrightarrow y$. The energies then becomes

$$E(J,M) = CJ(J+1) + (A-C)K^2. \tag{3.34}$$

For an asymmetric top rotor, $\mathrm{I}_a < \mathrm{I}_b < \mathrm{I}_c$, the Hamiltonian for the rotational motion is given in Eq. (1.1). The calculation of the eigenvalues for the asymmetric top rotor can be done in the symmetric top basis and the eigenvectors of the asymmetric top rotor are linear combinations of symmetric top wave functions. Referring to Eq. (6.66) and Eq. (6.67) in Zare [24], the diagonal elements for rotational matrix elements are

$$\begin{aligned} &\left\langle JKM\middle|J_x^2\middle|JKM\right\rangle = \left\langle JKM\middle|J_y^2\middle|JKM\right\rangle = \frac{1}{2}[J(J+1) - K^2], \\ &\left\langle JKM\middle|J_z^2\middle|JKM\right\rangle = K^2. \end{aligned} \tag{3.35}$$

The off-diagonal elements are

$$\begin{aligned} \left\langle JKM\middle|J_x^2\middle|JK\pm 2M\right\rangle =& -\left\langle JKM\middle|J_y^2\middle|JK\pm 2M\right\rangle \\ =& \frac{1}{4}\sqrt{J(J+1) - K(K\pm 1)}\sqrt{J(J+1) - (K\pm 1)(K\pm 2)}. \end{aligned} \tag{3.36}$$

In this thesis, the only asymmetric top molecule that is detailed studied is water. We work in the symmetric top basis set and make the axis identification $a \leftrightarrow y$, $b \leftrightarrow z$ and $c \leftrightarrow x$, this identification of axis is representation II^b in Zare [24].[2] The matrix elements of H_{Rotation} can be written as [24]

$$\begin{aligned} &\langle JKM|H_{\text{Rotation}}|JKM\rangle \\ =& \frac{(A+C)}{2}(J(J+1) - K^2) + BK^2, \end{aligned} \tag{3.37}$$

$$\begin{aligned} &\langle J, K+2, M|H_{\text{Rotation}}|JKM\rangle \\ =& \langle JKM|H_{\text{Rotation}}|J, K+2, M\rangle \\ =& \frac{(C-A)}{4}\sqrt{J(J+1) - K(K+1)}\sqrt{J(J+1) - (K+1)(K+2)}. \end{aligned} \tag{3.38}$$

[2] We worked in the representation II^b, because in this identification the dipole moment of water is along z-axis in the body-fixed frame.

Having the matrix elements for the rotational kinetic energy, we then show how to write the dipole-dipole interaction under mean-field approximation, i.e., $\cos\theta$ in the $|JKM\rangle$ basis. The dipole-dipole interaction under the mean-field approximation for symmetric top rotor and asymmetric top rotor can be calculated similarly.

$$\begin{aligned}\langle J'K'M'|\cos\theta|JKM\rangle &= \langle J'K'M'|\cos\theta|JKM\rangle \\ &= \sqrt{\frac{2J+1}{8\pi^2}}\sqrt{\frac{2J'+1}{8\pi^2}}\int [D^{J'}_{M'K'}(R)]^* \cos\theta D^{J}_{MK}(R)\, dR \\ &= \sqrt{\frac{2J+1}{8\pi^2}}\sqrt{\frac{2J'+1}{8\pi^2}}\int [D^{J'}_{M'K'}(R)]^* D^{1}_{00} D^{J}_{MK}(R)\, dR, \end{aligned} \tag{3.39}$$

where we express the dipole matrix elements in terms of integrals over products of winger-D matrix and use the fact that $\cos\theta = D^1_{00}$. Using the result of Eq. (B.3) and integral over a triple product of rotation matrices [24]

$$\begin{aligned}&\int D^{J_3'}_{M_3'M_3}(R)^* D^{J_2}_{M_2'M_2}(R) D^{J_1}_{M_{1'}M_1}(R)\, dR \\ =&\frac{8\pi^2}{2J_3+1}\langle J_1M_1, J_2M_2|J_3M_3\rangle \left\langle J_1M_1', J_2M_2'\middle| J_3M_3'\right\rangle . \end{aligned} \tag{3.40}$$

Eq. (3.39) can be written as

$$\begin{aligned}\langle J'K'M'|\cos\theta|JKM\rangle &= \sqrt{\frac{2J+1}{8\pi^2}}\sqrt{\frac{2J'+1}{8\pi^2}}\int D^{J'}_{M'K'}(R)^* D^{1}_{00} D^{J}_{MK}(R)\, dR \\ &= \sqrt{\frac{2J+1}{8\pi^2}}\sqrt{\frac{2J'+1}{8\pi^2}}\frac{8\pi^2}{2J'+1}\langle 10, JK|J'K'\rangle \langle 10, JM|J'M'\rangle \end{aligned} \tag{3.41}$$

Then, apply triangular inequality for the Clebsch-Gordan coefficient to Eq. (1.1)

$$\begin{aligned}&|1+J|, \geq J' \geq |1-J| \\ &K = K', \text{and } M = M'. \end{aligned} \tag{3.42}$$

The matrix elements of dipole-dipole interaction for symmetric and asymmetric rotors can be obtained [39].

$$\begin{aligned}&\langle J'K'M'|\cos\theta|JKM\rangle \\ =&\begin{cases} \sqrt{\frac{(J-K+1)(J+K+1)(J-M+1)(J+M+1)}{(2J+3)(J+1)^2(2J+1)}} & \text{if} \quad J'=J+1, \quad K'=K \quad \text{and} \quad M'=M, \\ \sqrt{\frac{(J-K)(J+K)(J-M)(J+M)}{(2J-1)J^2(2J+1)}} & \text{if} \quad J'=J-1, \quad K'=K \quad \text{and} \quad M'=M, \\ \frac{KM}{J(J+1)} & \text{if} \quad J'=J, \quad K'=K \quad \text{and} \quad M'=M. \end{cases} \end{aligned} \tag{3.43}$$

3.2.3 Angular momentum cutoff

To render the state space finite when performing the self-consistent diagonalization arising in the mean-field formalism, we introduce an angular momentum cutoff, $J_{\max}$, which we increase until convergence of the phase boundary is reached. Keeping $J_{\max} = 2, 3, 10, 15$ for the linear rotor and $J_{\max} = 2, 3, 5, 15$ for the symmetric rotor, we found that the phase boundary has no significant differences for τ less than 1. A larger $J_{\max}$ is needed to calculate the phase transition boundary at high temperatures, i.e., τ is much greater than 1, in the classical region.

At low temperatures, small $J_{\max}$ is enough to capture the order-disorder phase transition, because only several states are thermally populated. In this work, we focus on the order-disorder phase transition in the low-temperature region. Hence, we found it suitable to pick $J_{\max} = 10$ for the linear rotor and $J_{\max} = 5$ for the symmetric rotor.

3.3 Exact diagonalization results

This chapter aims to study the competition of kinetic energy and dipole-dipole potential and then construct the paraelectric-ferroelectric phase boundary. For completeness, all types of rotors are studied.

3.3.1 Phase diagrams for the different types of rotor

In this section, the phase diagram for the linear rotor, symmetric rotor, and asymmetric rotor constructed by solving self-consistent equation Eq. (3.9) following the iterative procedures introduced in Sec. 3.1.1 or by solving Eq. (3.16) from the free energy expression are shown. The results for these two ways are the same. For the first method, we consider FCC conventional lattice with periodic boundary condition and the system size, $L = 6$, that gives $4 \times 64 = 864$ lattice sites (FCC lattice has 4 sites per cell). We stop the iteration when the polarization difference in the two iteration steps is less than $10^{-}6$, which is good to capture the phase boundary.

Linear Rotor

We start with the linear rotor case. The phase diagram of linear dipolar molecules computed via mean-field theory is shown in Fig. 3.1. The figure's upper region is a paraelectric

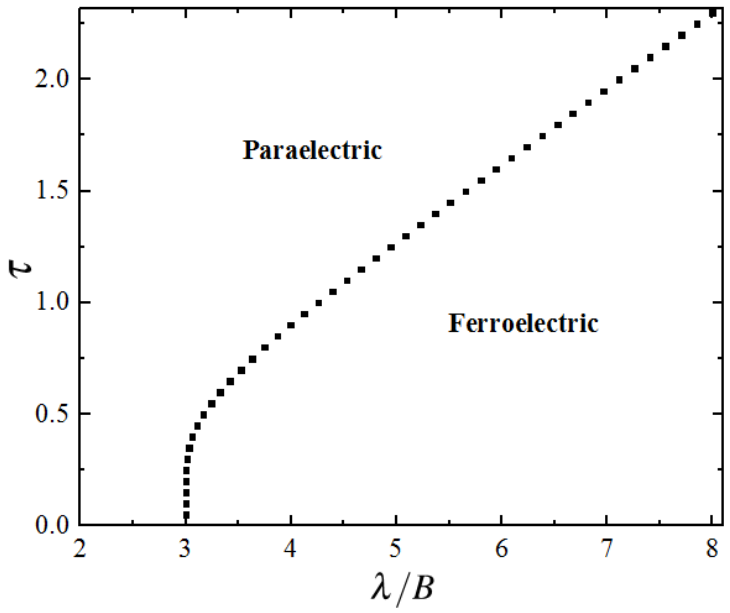

Figure 3.1: Phase diagram for linear rotor ($J_{\max} = 10$).The horizontal axis represents the strength of the dipole-dipole interaction and the vertical axis is dimensionless temperature $\tau \equiv k_{\mathrm{B}}T/B$. When $\tau = 0$, the quantum critical point is at $\lambda_c/B = 3$. The upper region of the figure is a paraelectric phase, while below the phase boundary is a homogeneous ferroelectric phase.

phase, while below the phase boundary is a homogeneous ferroelectric phase. It shows that the linear dipolar molecules at the ferroelectric phase have a phase transition, either increasing temperature or decreasing the strength of dipole-dipole interaction. The mean-field theory results of the ferroelectric phase do not have any orientational preference, i.e., dipoles can point in any direction. The quantum critical point can be understood by calculating the order parameter at zero temperature using perturbation theory.

$$\begin{aligned} p &= \left\langle \phi_n^{(1)} \middle| \cos\theta \middle| \phi_n^{(1)} \right\rangle, \\ &= \frac{\lambda p}{3B}, \end{aligned} \tag{3.44}$$

where $\phi_n^{(1)}$ is wave function of the ground state with the first order correction by perturbation theory and

$$\phi_n^{(1)} = |J=0, M=0\rangle + \frac{\lambda p}{2B}\frac{1}{\sqrt{3}}|J=1, M=0\rangle . \tag{3.45}$$

Re-arranging Eq. (3.44), we obtain $\lambda_c/B = 3$ at $\tau = 0$. To understand the slope of the phase diagram, we could calculate $\langle \cos\theta \rangle$ in the classical limit as

$$\langle \cos\theta \rangle = \frac{\iint \cos\theta \exp\{\beta\lambda p \cos\theta\} \sin\theta d\theta d\phi}{\iint \exp\{\beta\lambda p \cos\theta\} \sin\theta d\theta d\phi}, \tag{3.46}$$

Eq. (3.44) gives $p = \coth(\beta\lambda p) - \frac{1}{(\beta\lambda p)}$, and $\tau/\lambda = \frac{1}{3}$. It means that the slope of the phase boundary is approaching to $\frac{1}{3}$ as temperature increases. Having the phase diagram for the linear rotor, we then introduce the more general types of rotor, i.e., symmetric top and asymmetric top.

Symmetric rotor and asymmetric rotor

We next consider the symmetric top rotor and the basis we used is the oblate symmetric top basis as described in Eq. (3.31). A, B and C are rotational constants and C/A ratio indicates the shape of a rotor, i.e. pancake shape for a small C/A and cigar shape for a large C/A. As the C/A increases to infinite, we recover the linear rotor case.

The phase diagram for symmetric top rotor is shown in Fig. 3.2 for several different values of C/A. The quantum critical point is at $\lambda_c/A = 3$ for different C/A ratios. This can be showed in the same way as linear rotor case (see Eq. (3.44)). However, as temperature increases, we note qualitatively different boundaries and an interesting phenomenon of

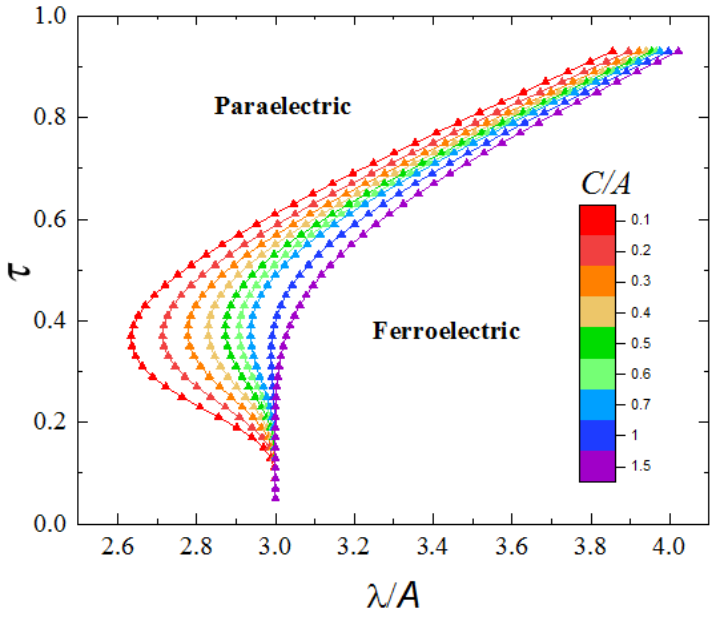

Figure 3.2: Phase diagram for the symmetric top rotor ($J_{\max} = 5$). The horizontal axis represents the strength of dipole-dipole interaction and the vertical axis is dimensionless temperature $\tau \equiv k_{\mathrm{B}}T/A$. The quantum critical point is at $\lambda_c/A = 3$. However, as temperature increases, the paraelectric and ferroelectric boundary bends towards weak interaction region and back.

reentrance [40] which occurs in the low temperature region, i.e., the phase boundary bends to the left then right and the phase of dipolar rotor system transforms from paraelectric into ferroelectric phases as temperature decreases and reenters into a paraelectric phase as temperature decreases further. The critical C/A for reentrance phenomenon occurs is 1.252. For a rotor in the deep prolate limit, i.e. $C/A \gg 1$, the phase diagram of the linear rotor (Fig. 3.1) is recovered, as expected. From Fig. 3.2, the quantum critical point is at $C/A = 3$ and independent of C/A. However, the special energy level structure which is characterized by rotational constants, i.e., C/A ratio of a rotor, results in a bending of the phase boundary and plays a role that makes the system easily ordered as the first several excited states become thermally populated and causes the reentrance. We shall return to the details of reentrance later.

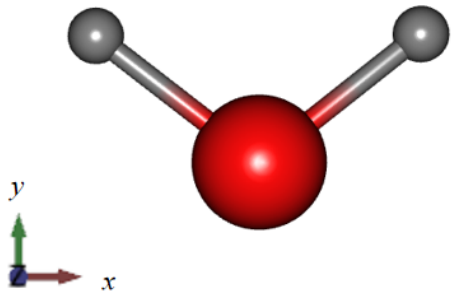

Figure 3.3: Water, in the xy-plane. The rotational constants A, B and C are the rotational constant for axis z, y and x in the figure.

Finally, we consider the most general case, the asymmetric top rotor whose three principal moments of inertia I_a, I_b and I_c, can be any real positive value. In general, the dipole moment can point along an arbitrary direction relative to the body axis. For concreteness reason, only water shape molecule is considered in this section. The rotational constants are: $A = 835840.288$ MHz, $B = 435351.717$ MHz and $C = 278138.7$ MHz [41].

The rotational Hamiltonian in the symmetric top basis is diagonal in quantum number J and M, thus needs only be solved in K blocks which have size $2J+1$ by $2J+1$ for each J level (see Appendix B). As no matrix elements couple between odd and even K states, states correspond to odd and even K blocks can be solved separately. The para states are from diagonalizing in the even K, while the ortho family is from diagonalizing in the odd K [24] (see Appendix C for more details).

The quantum critical point is not at the same position as linear and symmetric rotor cases. However, one can still calculate the position of quantum critical points similarly to

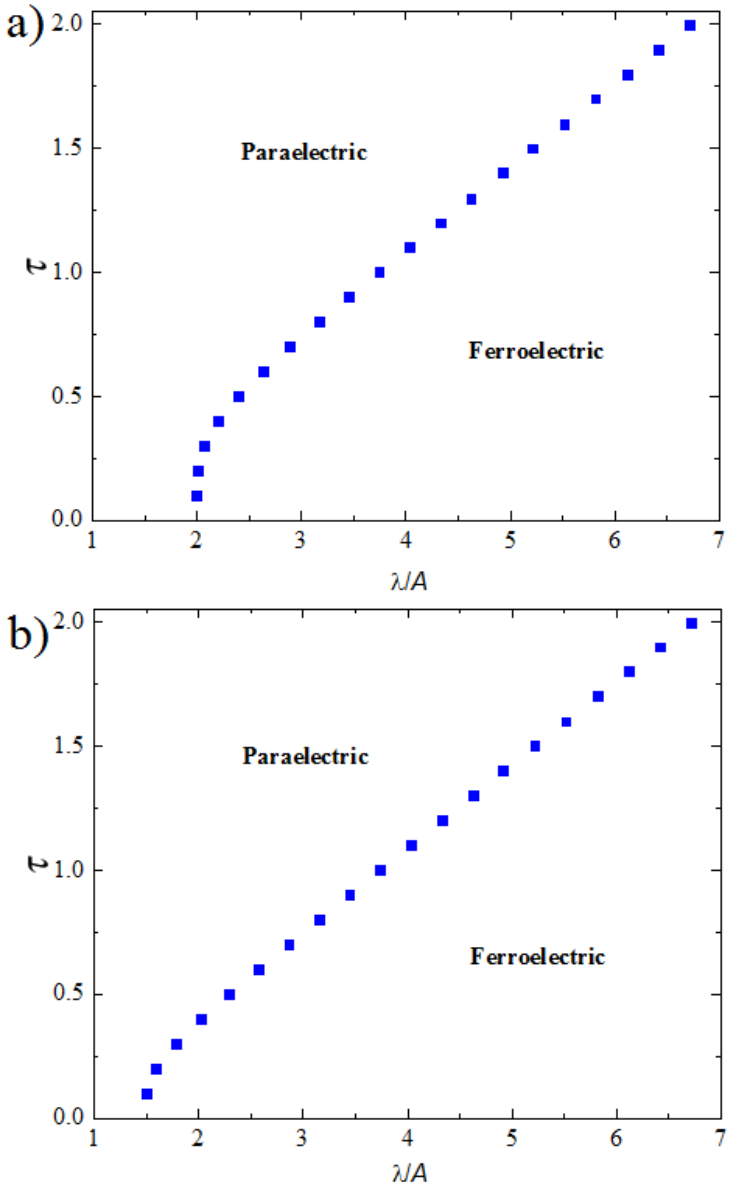

Figure 3.4: Phase diagrams for water shape rotor($J_{\max} = 5$). Water shape means that the asymmetric rotor has three rotational constants A, B and C, which is in the same ratio as water (water shape rotor). (a) ortho water. (b) para water.

the linear and symmetric cases. As can be seen, the quantum critical point is not the same for the ortho and para family in Fig. 3.4. The reason is that the ground state for the para water is a singlet and the ground states for the ortho water are triplet. The location of the quantum critical points shows that the ground states for ortho water have a stronger ordering tendency than para water.

3.3.2 Susceptibility and reentrance

In this section, we revisit the reentrance phenomenon in more detail. Reentrance is found in many systems, e.g., multi-component liquid mixtures [42] and anisotropic-planar-rotor model with a quadrupole-quadrupole interaction [43]. In our mean-field calculations, we also observed reentrant phases in symmetric rotors and asymmetric top rotors (see Fig 3.2 and Fig 3.8). We next will show how the thermal population of the rich spectrum structure leads to the reentrance phenomenon.

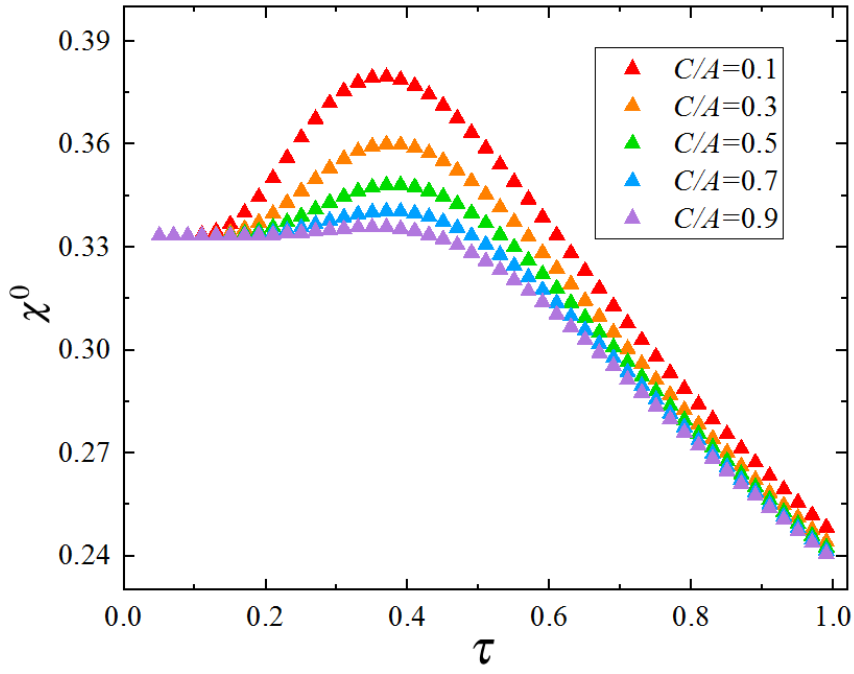

Figure 3.5: Non-interacting susceptibility $\chi^0 = 2k_BT(\frac{Z_2-Z_3}{Z_0})$ is plotted as function of dimensionless temperature $\tau \equiv k_BT/A$ for the symmetric rotor ($J_{max} = 5$).

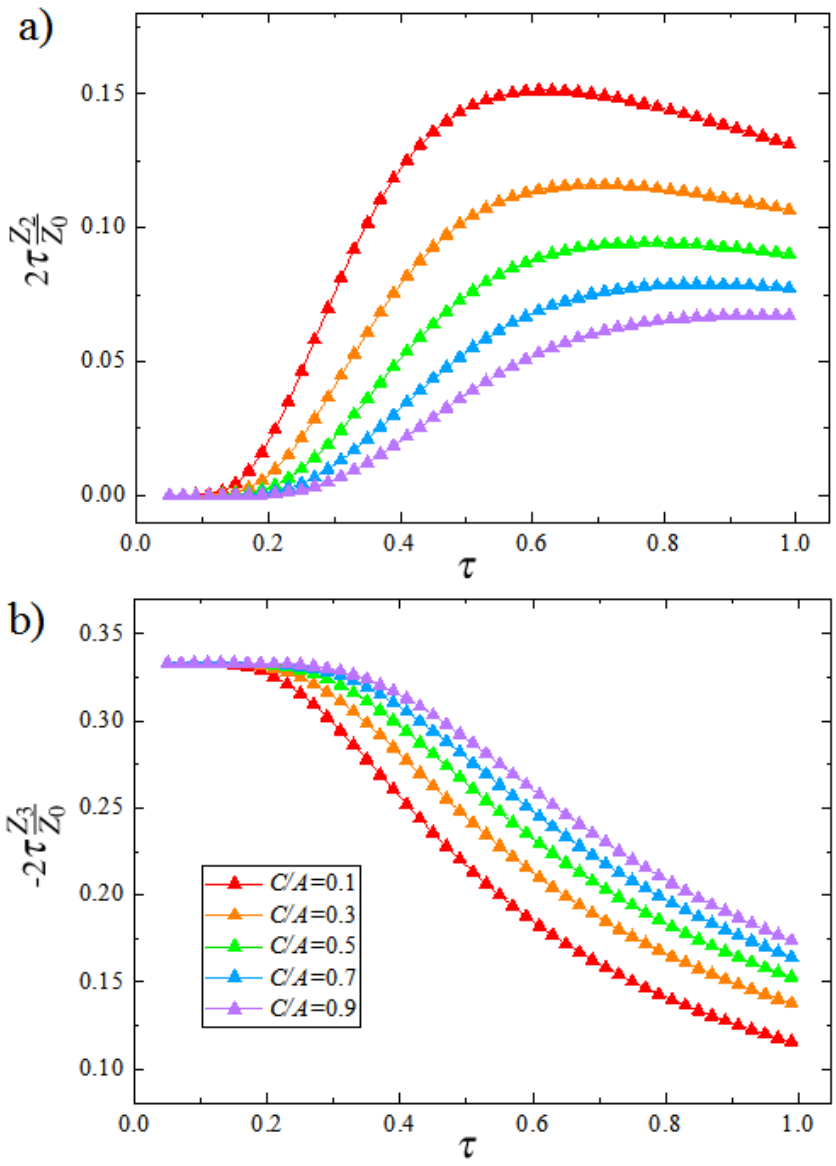

Figure 3.6: (a) First contribution ($2\tau\frac{Z_2}{Z_0}$) to the non-interacting susceptibility χ^0 ($J_{\max} = 5$). (b) Second contribution ($-2\tau\frac{Z_3}{Z_0}$) to the non-interacting susceptibility χ^0 ($J_{\max} = 5$), where $\tau \equiv k_{\mathrm{B}}T/A$ is dimensionless temperature.

We need to revisit the electric susceptibility in Eq. (3.21), as Eq. (3.21) contains the information of the shape of the phase boundary.

For a given λ, we have three different cases: no ferroelectric phase transition if Eq. (3.22) has no solution; there is ferroelectric transition if Eq. (3.22) has one solution; reentrance occurs if Eq. (3.22) has two solutions. To illustrate the three cases above, we plot the non-interacting susceptibility $\chi^0 = 2k_{\mathrm{B}}T(\frac{Z_2-Z_3}{Z_0})$ as a function of dimensionless temperature for different C/A ratios in Fig. 3.5, where Z_0, Z_2 and Z_3 are defined in Eq. (3.13). Two parts of $\chi^0 = 2k_{\mathrm{B}}T(\frac{Z_2-Z_3}{Z_0})$ are also plotted separately in Fig. 3.6. As can be seen in Fig. 3.5, the plot of $\chi^0(\tau)$ for the given C/A values has a local maximum, so Eq. (3.22) has two different critical temperatures for a specific given λ value where the electric susceptibility diverges, i.e.,

$$\chi^0(\tau_1) = \chi^0(\tau_2) = \frac{1}{\lambda}, \tag{3.47}$$

where τ_1 and τ_2 are two critical temperatures at which the electric susceptibility diverges.

Then we use energy level structure to understand the reentrance. The energy level structure for the symmetric top rotor is shown in Fig. 3.7. The energy in the same basis set as in Eq. (3.31) [24] has the from

$$E(J,K) = AJ(J+1) + (C-A)K^2. \tag{3.48}$$

As the rotational constant C increases, all states with the non-zero quantum number K shift upwards. Revisiting Eq. (3.13), Z_2 and Z_3 are temperature-dependent sums of first order correction squared and second order correction. The expression of the first order correction [39] in Z_2 is

$$E^{(1)}_{J,K,M} = \langle JKM|\cos\theta|JKM\rangle = \frac{MK}{J(J+1)}, \tag{3.49}$$

which implies that only states with $K \neq 0$ at all temperatures contribute to the Z_2 sum. So in Fig. 3.6 (a), $2k_{\mathrm{B}}T\frac{Z_2}{Z_0}$ is initially zero when $\tau = 0$ and increases to a peak as the $|J=1,K=1,M\rangle$ states thermal populated. Dipole operator only connects two states with the same quantum number K and M, but J differs by one. As the energy gap between states $|JKM\rangle$ and $|J+1,K,M\rangle$ increases as J increases, the ground state always gives the most significant contribution to the Z_3 sum. Hence, $-2k_{\mathrm{B}}T\frac{Z_3}{Z_0}$ in Fig. 3.6 (b) decreases as more and more states become thermally populated. As the rotational constant C increases, the energy of the state $|J=1,K=1,M\rangle$ also increases (see Fig. 3.7),

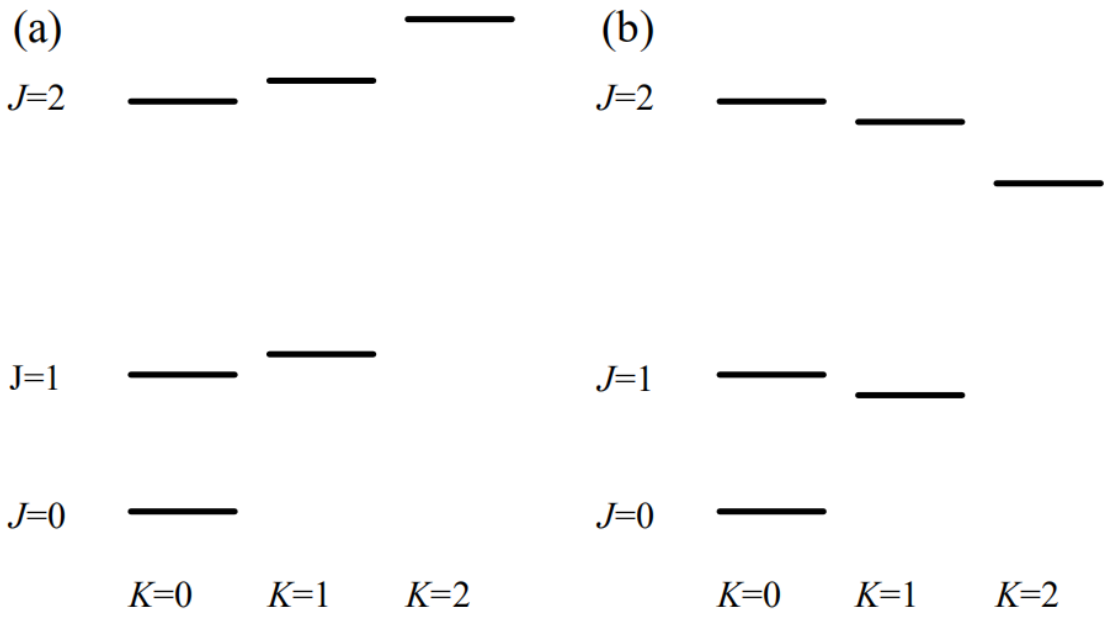

Figure 3.7: (a) Energy level structure for prolate top symmetric rotor ($C/A = 1.3$). (b) Energy level structure for oblate top symmetric rotor ($C/A = 0.7$). All levels with non-zero K are doubly degenerate.

and a higher temperature is needed to be thermally populated. Hence, the peak $2k_{\mathrm{B}}T\frac{Z_2}{Z_0}$ in Fig. 3.6 (a) appears at higher temperature and decreases in height and $-2k_{\mathrm{B}}T\frac{Z_3}{Z_0}$ in Fig. 3.6 (b) shifts upwards. For some special cases, i.e., $C/A \lesssim 1.252$ for which the χ^0 monotone decreases as a function of temperature, the stronger ordering tendency for the $|J = 1, K = 1, M\rangle$ state will win this competition, and the reentrance occurs.

Following the same logic, we can construct a similar argument for the asymmetric top rotor. Because of the stronger ordering tendency for the ortho ground states (see Fig. 3.8), i.e., para water has a singlet ground state and ortho water has the degenerate ground states, the quantum critical point of ortho water is smaller than the para water. For the mixed case or spinless water case, we construct the phase boundary with all rotational states and the phase boundary is close to the para water family but has a narrow reentrance region (see the black line in Fig. 3.8). It means that there are two different critical temperatures for a specific given λ value where the electric susceptibility diverges and so reentrance occurs.

In summary, a stronger ordering tendency for the rotational state with higher energy

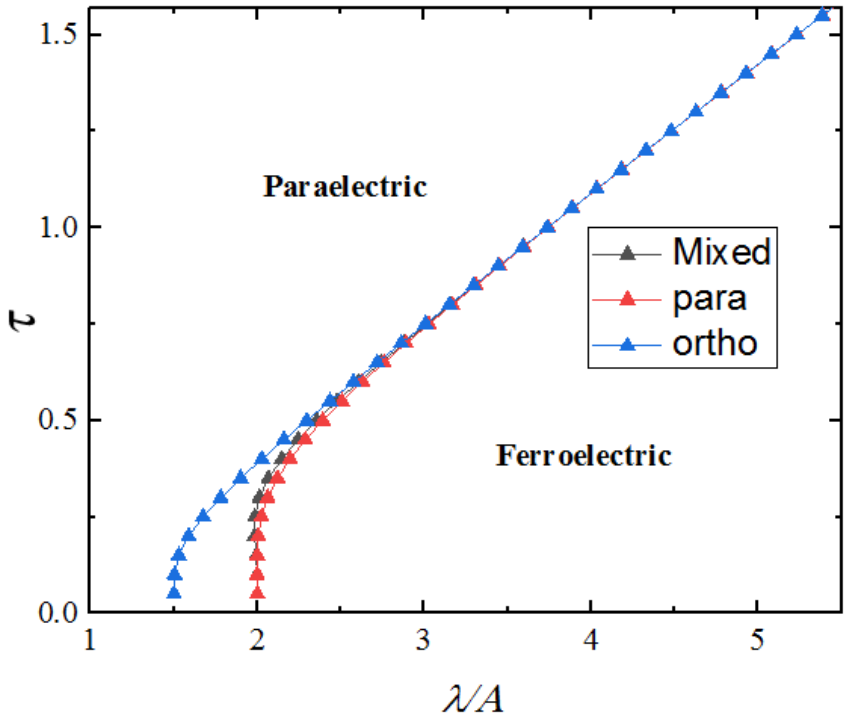

Figure 3.8: Phase diagrams for water ($J_{\max} = 5$), where $\tau = k_{\mathrm{B}}T/A$ is dimensionless temperature. Systems with pure para water, pure ortho water and the spinless water are shown.

causes the electric susceptibility to diverge at two different temperatures. Physically, the dipolar rotor system tends to be disordered as temperature increases. However, the special energy level structure (rotational constants) i.e., $C/A \lesssim 1.252$ for symmetric rotor and some of the asymmetric rotors, plays a role that makes the system easily ordered as the first several excited states become thermally populated and causes the reentrance.

3.4 Summary

In this chapter, we discuss the orientational order-disorder transition of dipolar rotors for the FCC lattice. The phase diagrams for the linear rotor, symmetric rotor, and asymmetric rotor were constructed by solving self-consistent equation Eq. (3.9) following the iterative procedures introduced in Sec. 3.1.1 and by solving Eq. (3.16) from the free energy expression. Reentrance occurs in the symmetric rotor and asymmetric rotor cases. We studied the reentrance by the electric susceptibility calculation, and we found the special energy level structure (rotational constants), i.e., $C/A \lesssim 1.252$ for symmetric rotor and some of the asymmetric rotors, plays a role that makes the system easily ordered as the first several excited states become thermally populated.

Chapter 4

Mean-field study of confined water molecules in beryl

Recently, water in both beryl and cordierite is reported to have a ferroelectric soft mode and exhibit the tendency towards a ferroelectric order. The dipolar coupling among the H_2O molecules confined in the beryl lattice has been argued to lead towards a ferroelectric state at low temperatures as suggested by the low-frequency dielectric measurements [17, 20]. However, the theoretical problem to consider in that case is more difficult than in the Buckminsterfullerene because of the strong crystal field due to the confinement and the partial occupation of H_2O molecules, i.e., some of the cages in beryl are empty. Furthermore, the existence of the impurity alkali ions (Li and Na) that produce a random electric field on the water molecules. The theoretical investigation of the electric behavior of water confined in beryl would be an interesting topic. The confined water molecules in beryl form a triangular lattice and water molecules are on the triangular lattice sites. In this chapter, we study the collective behavior of the triangular lattice using the mean-field method. We also ignore the translational motion of the trapped molecules and C_{60} cage's potential acting on the trapped water molecules.

We performed similar calculations as shown in Sec. 3.1. To simplify the general form of the mean-field Hamiltonian Eq. (3.3), we first need to know the ordered phase for the triangular lattice. In the following section, the ground state configuration of the dipoles for triangular lattice is studied using the iterative minimization method and the Luttinger-Tisza method introduced in Sec. 2.2.

4.1 Ground state configuration without crystal field

The crystal structure of beryl ($Be_3Al_2Si_6O_{18}$) contains channels of 5.1 Å in diameter which consists of six-membered rings of SiO_4 tetrahedra linked by AlO_6 octahedra and BeO_4 tetrahedra along c-axis(Fig. 1.3, panel (a)). The water molecules locate at the middle of the six-membered rings of SiO_4 tetrahedra and form a triangular lattice. At this point, we treat the water molecules as classical dipoles and ignore the crystal field. The ground state of the classical dipoles on the triangular lattice is investigated by the iterative minimization method and Luttinger-Tisza method. The translation and reciprocal lattice basis vectors for triangular lattice are [44]

$$\begin{aligned} &\mathbf{a_1} = (1,0,0) && \mathbf{a_2} = \frac{1}{2}(1,\sqrt{3},0) \quad \mathbf{a_3} = (0,0,c), \\ &\mathbf{b_1} = \frac{2\pi}{\sqrt{3}}(\sqrt{3},-1,0) && \mathbf{b_2} = \frac{2\pi}{\sqrt{3}}(0,2,0) \quad \mathbf{b_3} = \frac{2\pi}{c}(0,0,1). \end{aligned} \tag{4.1}$$

For water in the beryl case, c/a is equal to 0.5. The dipoles are given full rotational freedom, i.e., three-component dipoles of fixed length.

4.1.1 Iterative minimization method

We start with $6\times6\times6$ dipoles with fixed length on the triangular lattice pointing in random directions with the periodic boundary condition. Then, we perform the iteration procedures introduced in Sec. 2.2.1. The electric field used in the iteration steps is calculated by Ewald method[34] (Appendix A). The loop stops when the difference between the energy of the new set ($(i+1)^{th}$ loop) of dipole vectors and the old set (i^{th} loop) is smaller than 10^{-5}, i.e.,

$$|E_{i+1} - E_i| < 10^{-5}. \tag{4.2}$$

We found the ground state for dipoles in triangular lattice depends on c/a ratios. The ground state configurations are summarized below:
1. Half of the dipoles are up, and another half of dipoles are down in the XY plane, and the other layers are copies of the xy plane when $c/a < 0.96$, and we call this state a staggered phase.
2. Dipoles have ferroelectric order in XY plane but flip the direction in their neighbor plane when $c/a > 0.96$, and we refer to this state as planar ferro/anti-ferro phase.

This procedure does not find the true ground state for some initial conditions. Sometimes the dipoles are trapped in some local minima with close energy to the true ground state introduced above.

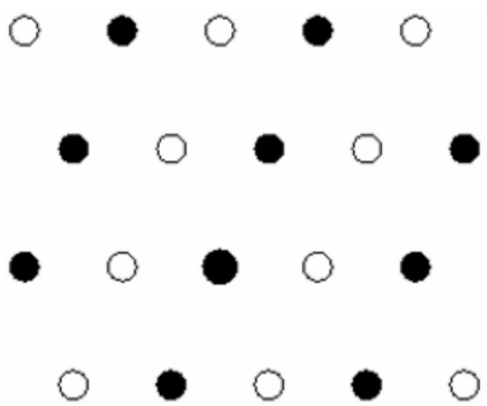

Figure 4.1: Top view of the ground state configurations for dipoles in triangular lattice for $c/a < 0.96$.

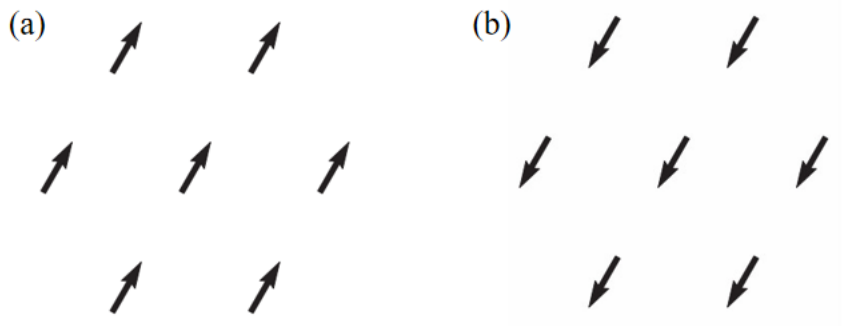

Figure 4.2: Top view of the ground state configurations for dipoles in triangular lattice for $c/a > 0.96$. (a) and (b) are the two neighbor planes.

4.1.2 Luttinger-Tisza Method

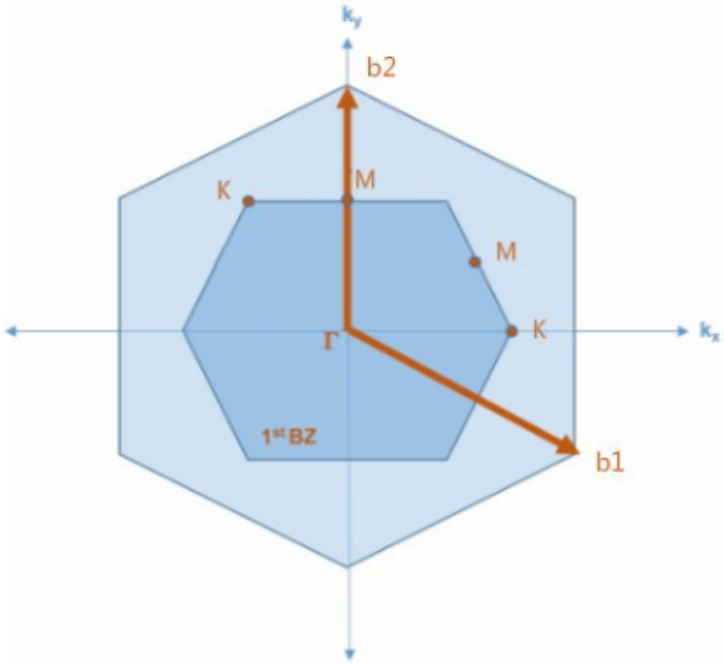

Figure 4.3: Top view of the first Brillouin zone of the triangular lattice. Some of the special points are shown. Γ is at the center of the first Brillouin zone, and K point and M point are at the first Brillouin zone boundary.

In this section, Luttinger-Tisza (TL) method [26, 29] is applied to the triangular lattice. We wrote the dipole-dipole interaction Hamiltonian Eq. (2.2) as a sum of the Fourier transform of the interactions over all wavevectors $\mathbf{q}$ following the procedures introduced in Sec. 2.2.2, then diagonalize the interaction Hamiltonian to find eigenvalues in the first Brillouin zone (see Fig. 4.3). The Fourier transform of the interaction matrix is shown in Appendix A.

From Fig. 4.4(a), there is a flat band from the Γ point to the M point for $c/a = 0.5$ (the flat band is plotted in Fig. 4.5). The eigenvalues are very close in this region and the global minimum is at K point ($\lambda_{\mathrm{K}} = -19.23523$ and $\lambda_{\mathrm{M}} = -19.23446$). The normalized eigenvector for $\lambda_{\mathrm{K}} = -19.23523$ is (0,0,1) which means that if the ordering wavevector is $\mathbf{q}^* = \mathbf{q}_{\mathrm{K}}$, all dipoles correspond $\mathbf{q}^* = \mathbf{q}_{\mathrm{K}}$ ground state only have z-component, i.e., $\mathbf{s_i} = \hat{z}$ or $\mathbf{s_i} = -\hat{z}$. This means if $\mathbf{q}^* = \mathbf{q}_{\mathrm{K}}$ is the ordering wavevector, the configuration can be written as $\mathbf{s_i} = \cos(\mathbf{q}_{\mathrm{K}} \cdot \mathbf{r_i})\ \hat{\mathbf{z}}$ according to Eq. (2.21) and $\mathbf{q}_K \cdot \mathbf{R_i}$ has to equal

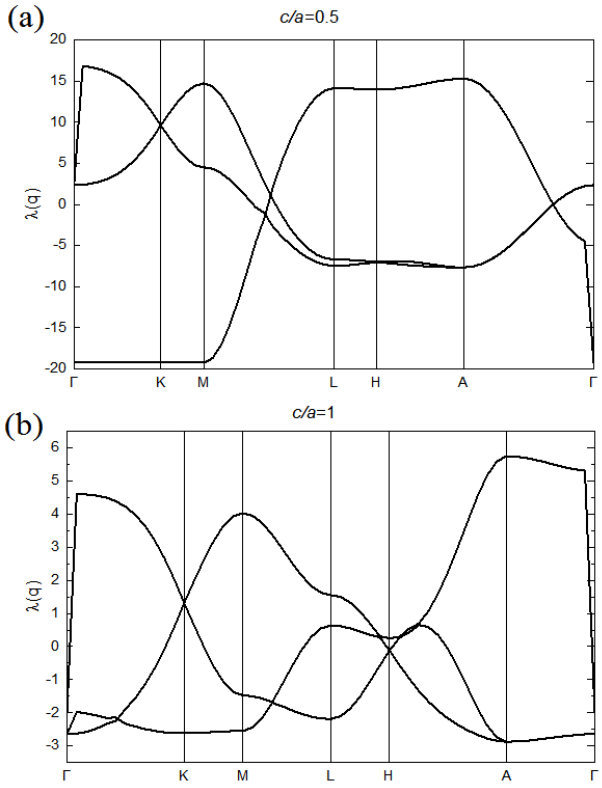

Figure 4.4: Luttinger-Tisza eigenvalues plotted in the Brillouin zone of the triangular lattice for $c/a = 0.5$ and $c/a = 1$.

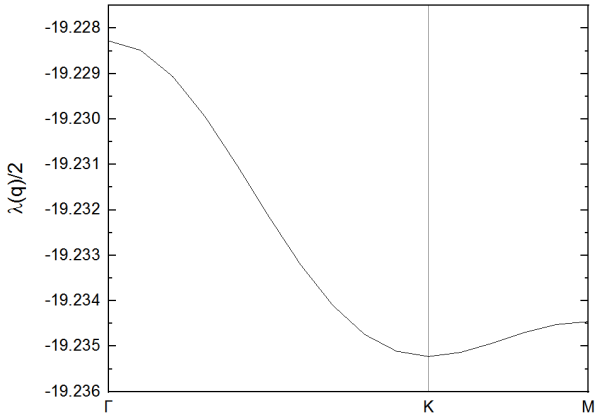

Figure 4.5: The flat band in Fig. 4.4(a) from Γ point to M point for $c/a = 0.5$.

to $n\pi$, where n is an integer. However, $\mathbf{q}_{\mathrm{K}} \cdot \mathbf{R_i} \neq n\pi$ and $\mathbf{q}^* = \mathbf{q}_{\mathrm{K}}$ is not the ordering wavevector. $\mathbf{q}^* = \mathbf{q}_{\mathrm{M}}$ with a higher energy has the normalized eigenvector (0,0,1). In this case, the strong condition is fulfilled, i.e., the dipole is fixed to a unit length, and we find $\mathbf{q}^* = \mathbf{q}_{\mathrm{M}}$ is the staggered phase found by the iterative minimization method. The energy ($\lambda_{\mathrm{M}} = -19.23446$) calculated in both methods are the same.

From Fig. 4.4(b), the global minimum is at A point with energy $\lambda_{\mathrm{A}} = -2.87114$ and a normalized eigenvector (0,0,1). The strong condition is fulfilled, i.e., the dipole is fixed to a unit length, for $\mathbf{q}^* = \mathbf{q}_{\mathrm{A}}$. So $\mathbf{q}_{\mathrm{A}}$ is the ordering wavevector that corresponds to a planar ferro/anti-ferro phase we found by the iterative minimization method.

In summary, we found that the ground state of dipoles for triangular lattice depends on the c/a ratio. The iterative minimization method and Luttinger-Tisza method showed that the ground state is a staggered phase for $c/a < 0.96$ and a planar ferro/anti-ferro phase for $c/a > 0.96$. Having this information, we then repeat the same procedure as in Chapter. 3 in the following sections.

4.2 Mean-field Hamiltonian of the triangular lattice

Due to the complexity of the diagonalization, a linear rotor is considered in this section. Fellow the same procedure introduced in Sec. 3.1, we have a similar treatment to the dipole-dipole interaction term. We start with Eq. (3.3). For $c/a < 0.96$, we may have a staggered phase when the dipole-dipole interaction is strong. The average polarization as order parameter is along Z-direction in lab frame, i.e. $p_i \equiv \langle n_i^Z \rangle = \langle \cos\theta_i \rangle$ when the dipole-dipole interaction is significantly strong. This way, we have

$$H_{\mathrm{MF}} = \sum_i^N \left[B\mathbf{J}^2 - \lambda_i (p_i \cos\theta_j - \frac{1}{2} p_i p_j) \right], \tag{4.3}$$

where we have defined the dipolar lattice sum as $\lambda_i \equiv -D\sum_j (-1)^j \Lambda_{ij}^{ZZ}$.

For $c/a > 0.96$, we may have a planar ferro/anti-ferro phase when the dipole-dipole interaction is strong. We assume the polarization in the XY-plane is along the X-direction, and the average polarization is $p_i \equiv \langle n_i^X \rangle = \langle \sin\theta_i \cos\phi_i \rangle$. This way, we have

$$H_{\mathrm{MF}} = \sum_i^N \left[B\mathbf{J}^2 - \lambda_i (p_i \sin\theta_j \cos\phi_j - \frac{1}{2} p_i p_j) \right], \tag{4.4}$$

where we have defined the dipolar lattice sum as $\lambda_i \equiv -D\sum_j (-1)^n \Lambda_{ij}^{ZZ}$ (n is the index of the XY-plane).

Thus, we convert a confined interacting dipolar rotors problem to a single dipolar rotor in an effective electric field problem, and combining the appropriate matrix elements and numerically exact diagonalizations derived later, we can solve $p_i = \langle \cos\theta_i \rangle$ for $c/a > 0.96$ and $p_i = \langle \sin\theta_i \cos\phi_i \rangle$ for $c/a > 0.96$ in a self-consistent manner as shown in Sec. 3.1.1.

4.3 Exact diagonalization

The basis set functions for the linear rotor have been introduced in Sec. 3.2.1. In this section, the details of writing the dipole-dipole interaction under mean-field approximation will be introduced i.e., $\cos\theta$ and $\sin\theta\cos\phi$ in the $|JM\rangle$ basis.

The matrix elements for $\cos\theta$ have been derived in Eq. (3.30) and we only need to find matrix elements for $\sin\theta\cos\phi$. We first write $\cos\theta$ in a sum of spherical harmonics [24]

$$\sin\theta\cos\phi = \sqrt{\frac{2\pi}{3}}(-Y_1^1(\theta,\phi) + Y_1^{-1}(\theta,\phi)). \tag{4.5}$$

Then, we write the matrix elements of $Y_1^1(\theta,\phi)$ and $Y_1^1(\theta,\phi)$ in term of integrals over products of spherical harmonics [24]

$$\begin{aligned}\langle J'M'|Y_1^1(\theta,\phi)|JM\rangle &= \iint [Y_{J'}^{M'}(\theta,\phi)]^* Y_1^1(\theta,\phi) Y_J^M(\theta,\phi)\, d\theta\, d\phi \\ &= \sqrt{\frac{3(2J+1)}{4\pi(2J'+1)}}\, \langle J0;10|J'0\rangle \, \langle JM;11|J'M'\rangle\,, \end{aligned} \tag{4.6}$$

$$\begin{aligned}\langle J'M'|Y_1^{-1}(\theta,\phi)|JM\rangle &= \iint [Y_{J'}^{M'}(\theta,\phi)]^* Y_1^{-1}(\theta,\phi) Y_J^M(\theta,\phi)\, d\theta\, d\phi \\ &= \sqrt{\frac{3(2J+1)}{4\pi(2J'+1)}}\, \langle J0;10|J'0\rangle \, \langle JM;1-1|J'M'\rangle\,. \end{aligned} \tag{4.7}$$

Combining Eq. (4.6) and Eq. (4.7)together

$$\begin{aligned}
&\langle J'M'|-dE\sin(\theta)\cos(\phi)|JM\rangle \\
&= \begin{cases}
-\sqrt{\frac{(J+M+1)(J+M+2)}{4(2J+3)(2J+1)}} & \text{if} \quad J'=J+1 \quad \text{and} \quad M'=M+1, \\
\sqrt{\frac{(J-M+1)(J-M+2)}{4(2J+1)(2J+3)}} & \text{if} \quad J'=J+1 \quad \text{and} \quad M'=M-1, \\
\sqrt{\frac{(J-M-1)(J-M)}{4(2J-1)(2J+1)}} & \text{if} \quad J'=J-1 \quad \text{and} \quad M'=M+1, \\
-\sqrt{\frac{(J+M)(J+M-1)}{4(2J-1)(2J+1)}} & \text{if} \quad J'=J-1 \quad \text{and} \quad M'=M-1,
\end{cases}
\end{aligned} \tag{4.8}$$

we obtain the matrix elements of $\sin\theta\cos\phi$.

4.4 Exact diagonalization results

The aim of this chapter is to study the competition of the kinetic energy and dipole-dipole interaction for triangular lattice, and construct the order-disorder phase boundary. The phase diagram for the linear rotor constructed by solving $p_i = \langle\cos\theta_i\rangle$ for $c/a > 0.96$ and $p_i = \langle\sin\theta_i\cos\phi_i\rangle$ for $c/a > 0.96$ following the iterative procedures introduced in Sec. 3.1.1 or by solving Eq. (3.16) from the free energy expression. For the first method, we consider triangular lattice with the periodic boundary condition and the system size, $L = 6$, that gives 216 lattice sites. The results for these two ways are the same.

The phase diagram of the linear rotor computed via mean-field theory is shown in Fig. 4.6. In Fig. 4.6, the ordered phase is a staggered phase for $c/a < 0.96$ and a planar ferro/anti-ferro phase for $c/a > 0.96$. To see the role of the c/a played in the Fig. 4.6, we revisit the definition of the dipolar lattice sum in Eq. (4.3) and Eq. (4.4), i.e., $\lambda_i \equiv -D\sum_j(-1)^j\Lambda_{ij}^{ZZ}$ for $c/a < 0.96$ and $c/a > 0.96$ for $\lambda_i \equiv -D\sum_j(-1)^n\Lambda_{ij}^{ZZ}$, where $D \equiv \frac{d^2}{4\pi\epsilon_0}$. If we fix the D in the dipolar lattice sum and Fig. 4.6 can be re-constructed in a different manner (see Fig. 4.7). Fig. 4.6 and Fig. 4.7 present the same phase diagram but in the differnt way. In Fig. 4.7, it can be seen that there is no planar ferro/anti-ferro phase when D is small, e.g., Fig. 4.7(a), and there is a a staggered phase for $c/a < 0.96$ and a planar ferro/anti-ferro phase for $c/a > 0.96$ when D is large, e.g., Fig. 4.7(b).

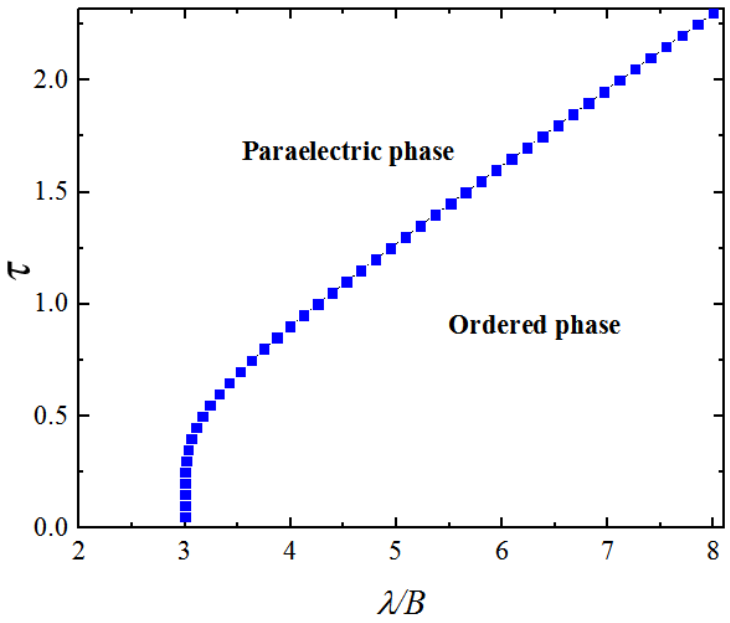

Figure 4.6: Phase diagram for linear rotor ($J_{\max} = 10$).The horizontal axis represents the strength of the dipole-dipole interaction and the vertical axis is dimensionless temperature $\tau \equiv k_{\mathrm{B}}T/B$. When $\tau = 0$, the quantum critical point is at $\lambda_c/B = 3$. The ordered phase is a staggered phase for $c/a > 0.96$ and a planar ferro/anti-ferro phase for $c/a > 0.96$.

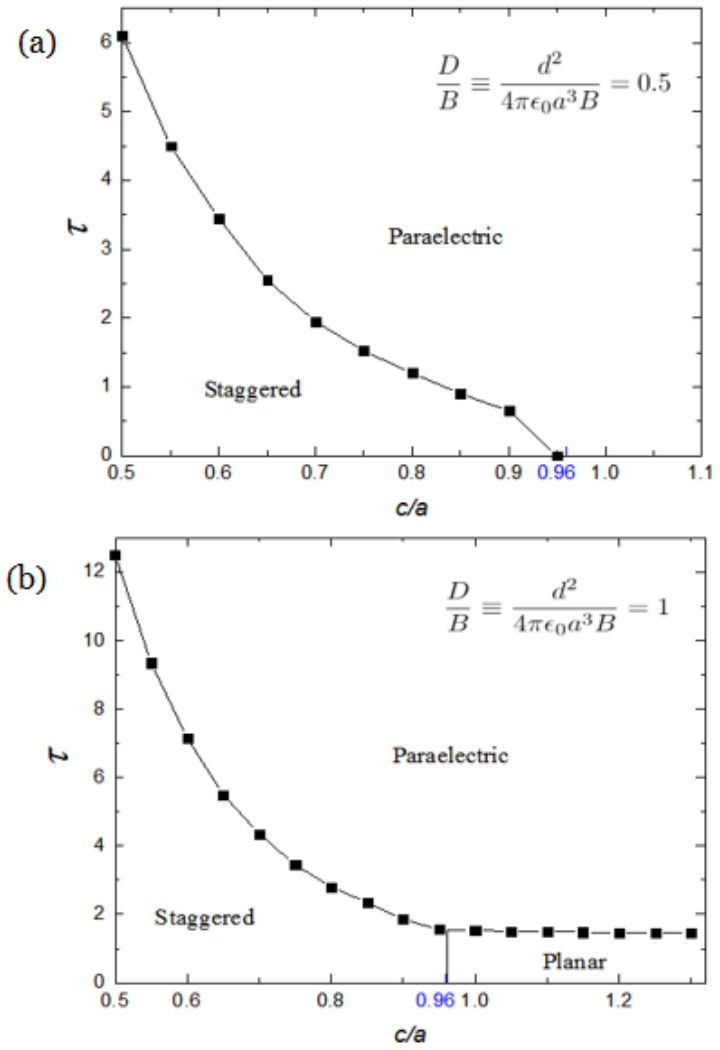

Figure 4.7: Phase diagram for linear rotor ($J_{\max} = 10$).The horizontal axis is c/a ratio and the vertical axis is dimensionless temperature $\tau \equiv k_{\mathrm{B}}T/B$. The dimensionless quantity D/B is 0.5 for (a) and 1 for (b).

4.5 Summary

In this chapter, we discuss the orientational order-disorder transition of dipolar rotors for triangular lattice. First, the ground state of the triangular lattice is found to be a staggered phase for $c/a < 0.96$ and a planar ferro/anti-ferro phase for $c/a > 0.96$. Then, the mean-field approximation for the dipole-dipole interaction and the exact diagonalization is introduce. Finally, phase diagrams for the linear rotor were constructed by solving $p_i = \langle \cos\theta_i \rangle$ for $c/a < 0.96$ and $p_i = \langle \sin\theta_i \cos\phi_i \rangle$ for $c/a > 0.96$ following the iterative procedures introduced in Sec. 3.1.1.

Chapter 5

Materials Context

5.1 Application of the present work

In Chapter 3 and Chapter 4, we have discussed the orientational order-disorder transition of dipolar rotors for FCC lattice and triangular lattice. In this section, we revisit the phase diagrams and show how to locate some specific molecules in the phase diagram.

5.1.1 Confined dipolar molecule in Buckminsterfullerene

The horizontal axis of Fig. 3.1 and Fig. 3.2 represent the strength of dipole-dipole interaction, which is characterized by the dipole moment, lattice structure, and rotational constants. Once we know the dipole moment, lattice structure, and rotational constants, we can locate a lattice into the phase diagram and predict if there is a spontaneous ferroelectric order. The ratio of λ/B ($\lambda_i \equiv -D\sum_j \Lambda_{ij}^{ZZ}$ defined in Eq. (3.5)) of the endofullerenes for linear molecules can be calculated using

$$\begin{aligned} \frac{\lambda}{B} &= -D\sum_j \Lambda_{ij}^{ZZ}, \\ &= \frac{d^2}{4\pi\epsilon a^3 B}(\frac{16\pi}{3}). \end{aligned} \tag{5.1}$$

where d is the screened dipole moment given by the DF-MP2 method[45] (see Table 5.1), a is the lattice constants for C_{60} lattice (we use $a = 14.17$Å for C_{60} at 300 K [3]) and $-\frac{16\pi}{3}$ is $\sum_j \Lambda_{ij}^{ZZ}$ for FCC lattice. This number can be checked by the Ewald summation

Table 5.1: Properties of endofullerenes computed using *ab initio* methods for the case of the molecule's center of mass being at the center of the C_{60} cage [1]

Property	Method	HF	NaF	NaCl	LiF	LiCl	H_2O	NH_3
Dipole moment (Debye)	DF-MP2	**0.52**	**2.02**	**2.61**	**1.82**	**1.99**	**0.54**	**0.46**

Table 5.2: Properties of endofullerenes computed using mean-field theory. The quantum critical value in the fourth column is the calculated λ/B value for the linear rotor (λ/A for the symmetric and asymmetric rotor). The MF-T_c in the fifth column is the dimensionless mean-field critical temprature for the paraelectric-ferroelectric phase transition.

Class	Guest molecule	Quantum critical value	Location	MF-T_c
Linear	HF	0.38	Paraelectric	-
	LiF	73.07	Ferroelectric	24.46
	LiCl	166.03	Ferroelectric	53.50
	NaF	285.47	Ferroelectric	90.37
	NaCl	927.22	Ferroelectric	285.60
Symmetric	NH_3	0.66	Paraelectric	-
Asymmetric	H_2O	0.31	Paraelectric	-
	D_2O	0.56	Paraelectric	-

method [34, 46]. One can locate the calculated λ/B on the phase diagram to determine whether a spontaneous ferroelectric phase transition is expected. For HF@C_{60}, NH_3@C_{60} and H_2O@C_{60}, the calculated λ/B are 0.38, 0.66 and 0.31, and locate at the paraelectric region. LiF@C_{60}, LiCl@C_{60}, NaF@C_{60} and NaCl@C_{60}, whose λ/B values are 73.07, 166.03, 285.47 and 927.22 located at ferroelectric region, are predicted to have a phase transition at 24.46, 53.5, 90.37 and 285.6. The results are summarized in Table 5.2.

In the Table 5.2, HF@C_{60} and H_2O@C_{60} have been synthesized by molecular surgery [2, 12] and have not found a ferroelectric ordered experimentally. The rest molecules have not been inserted into C_{60}. Our results suggest that LiF@C_{60}, LiCl@C_{60}, NaF@C_{60} and NaCl@C_{60} have a ferroelectric-paraelectric phase transition as temperature increases.

5.1.2 Confined water molecules in beryl

In Chapter 4, we found the ground state for dipoles of the triangular lattice is a staggered phase for $c/a = 0.5$ ($c/a = 0.5$ is the ratio of confined water in beryl). However, the water molecules in beryl are found pointing in the *ab*-plane. To understand the collective

behavior of water molecules in beryl, we also need to consider a six-fold planar potential well due to the confinement. The six-fold planar potential is discussed in Ref. [6, 20, 21]. This six-fold planar potential forces the dipole moment of water molecules to point in one of the six equivalent positions in the *ab*-plane. So our model, which only considered the rotational part of kinetic energy and the dipole-dipole interaction, is not sufficient to understand the confined water molecules in beryl.

5.2 Summary

In this chapter, we discussed the application of our results. We can locate some specific molecules in our phase diagram to make a prediction if there is a ferroelectric phase transition. For confined dipolar molecules in C_{60}, our results suggest that $LiF@C_{60}$, $LiCl@C_{60}$, $NaF@C_{60}$ and $NaCl@C_{60}$ are potential ferroelectric materials. For confined water molecules in beryl, we need to add a term for the six-fold planar potential in our current model [6, 20, 21].

Chapter 6

Conclusion

6.1 Conclusion of present work

In this work, we have discussed the orientational phase transition of confined quantum molecules in the quantum dipolar rotor model. We focus on confined dipolar molecules in C_{60} and confined water molecules in beryl. We used the simplest possible Hamiltonian composed of the rotational term and dipole-dipole interaction term to encapsulate the main features of the confined dipolar molecules. The rotational term and dipole-dipole interaction term do not commute with each other, and the competition of these two terms leads to an orientational order-disorder phase transition. The method we used is the mean-field method. We applied mean-field approximation to the dipole-dipole interaction and obtained the mean-field Hamiltonian of our model. We simplified the mean-field Hamiltonian according to the ground state configuration favored by the dipole-dipole interaction. We used two methods, i.e., the iterative minimization method and the Luttinger-Tisza method, to search the ground state configuration. After having the appropriate matrix elements and numerically exact diagonalizations, we constructed the phase diagrams by solving self-consistent equations and solving Eq. (3.16) from the free energy expression.

For confined dipolar molecules in C_{60}, we constructed the phase diagram for the linear rotor, symmetric rotor, and asymmetric rotor. The ordered phase was found to be the ferroelectric phase. We found that reentrance happens for the symmetric rotor and asymmetric rotor cases, and we calculated electric susceptibility to understand the reentrance. The reason for the reentrance has been identified because of the special energy level structure that results in the bending of the phase boundary. It plays a role that makes the system easily ordered as the first several excited states become thermally populated.

We found the ordered phase for confined water molecules in beryl is a staggered phase when $c/a = 0.5$ in our model. However, the dipole moment of water molecules was found in the ab-plane experimentally due to a six-fold potential [6, 19, 20, 21]. This suggests that our model is not enough to describe the confined water molecules' behavior in beryl, and one more term for the six-fold potential has to be added in our model.

We discussed the application of our results in Chapter 5. We locate some specific molecules in our phase diagram to predict if there is a ferroelectric phase transition (see Table 5.2). For confined dipolar molecules in C_{60}, our results predict that LiF@C_{60}, LiCl@C_{60}, NaF@C_{60} and NaCl@C_{60} are potential ferroelectric materials.

6.2 Future Directions

In this work, we used the simplest dipolar rotor model to study confined dipolar molecules' collective behavior. We ignore the cage's crystal field of the confined dipolar molecules. In fact, the rotational motion of the confined molecule would be affected by the potential energy that the confined molecule experiences due to the confinement, i.e., the rotational degeneracy of the energy spectrum of the confined molecule is lifted for C_{60} case [47], and the dipoles are forced in the ab-plane for water in beryl, which does not agree with our current results. To accurately capture the dielectric property of the confined dipolar molecules, the potential term needs to be added. The potential can be written as a series of spherical harmonics physically based on the symmetry of the system and fitting into IR spectra to obtain the coefficients of the spherical harmonics. Especially for the water in beryl, a phase diagram can be constructed as a function of the strength of the potential follow the steps we discussed in Chapter 3 and Chapter 4 and we then can locate the beryl with water in this phase diagram.

References

[1] Bo Liu, J. G. Rau, Y. N. Kalugina, and Michel J. P. Gingras. Mean-field theory of ferroelectric order of quantum dipolar rotors on the face-centered cubic lattice: Application to molecular dipoles in endohedral C_{60}. (unpublished), 2020.

[2] K. Komatsu. Encapsulation of molecular hydrogen in fullerene C_{60} by organic synthesis. *Science*, 307:238–240, 2005.

[3] Shinobu Aoyagi *et al.* A cubic dipole lattice of water molecules trapped inside carbon cages. *Chem. Commun.*, 50:524–526, 2014.

[4] Sally Bloodworth *et al.* First synthesis and characterization of $CH_4@C_{60}$. *Angewandte Chemie International Edition*, 58:5038–5043, 2019.

[5] Jerzy Cioslowski and Asiri Nanayakkara. Endohedral fullerites: A new class of ferroelectric materials. *Phys. Rev. Lett.*, 69:2871–2873, 1992.

[6] B. P. Gorshunov et al. Incipient ferroelectricity of water molecules confined to nanochannels of beryl. *Nature Communications*, 7, 2016.

[7] M. A. Belyanchikov *et al.* Dielectric ordering of water molecules arranged in a dipolar lattice. *Nature Communications*, 11, 2020.

[8] H. W. Kroto, J. R. Heath, S. C. O'Brien, R. F. Curl, and R. E. Smalley. C_{60}: Buckminsterfullerene. *Nature*, 318:162–163, 1985.

[9] Frank Rioux. Quantum mechanics, group theory, and C_{60}. *Journal of Chemical Education*, 71:464, 1994.

[10] M. S. Dresselhaus, G. Dresselhaus, and P. C. Eklund. *Science of fullerenes and carbon nanotubes: their properties and applications.* Academic Press, 1996.

[11] Yan Chai *et al.* Fullerenes with metals inside. *The Journal of Physical Chemistry*, 95:7564–7568, 1991.

[12] K. Kurotobi and Y. Murata. A single molecule of water encapsulated in fullerene C_{60}. *Science*, 333:613–616, 2011.

[13] Andrea Krachmalnicoff *et al.* The dipolar endofullerene HF@C_{60}. *Nature Chemistry*, 8:953–957, 2016.

[14] Takeo Oku. Hydrogen storage in boron nitride and carbon nanomaterials. *Proceedings of 1st International e-Conference on Energies*, 2014.

[15] Beata Szefler. Nanotechnology, from quantum mechanical calculations up to drug delivery. *International Journal of Nanomedicine*, Volume 13:6143–6176, 2018.

[16] Carlo Beduz *et al.* Quantum rotation of ortho and para-water encapsulated in a fullerene cage. *PNAS*, Volume 109:12894–12898, 2012.

[17] Martin Dressel, Elena S. Zhukova, Victor G. Thomas, and Boris P. Gorshunov. Quantum electric dipole lattice. water molecules confined to nanocavities in beryl. *Journal of Infrared, Millimeter, and Terahertz Waves*, 39:799–815, 2018.

[18] Gilberto Artioli, Romano Rinaldi, Kenny Stahl, and Pier Francesco Zanazzi. Structure refinements of beryl by single-crystal neutron and X-ray diffraction. *American Mineralogist*, 78:762–768, 1993.

[19] G. Diego Gatta, F. Nestola, G.D. Bromiley, and S. Mattauch. The real topological conÞ guration of the extra-framework content in alkali-poor beryl: A multimethodological study. *American Mineralogist*, 91:29 – 34, 2006.

[20] Alexander I. Kolesnikov *et al.* Quantum tunneling of water in beryl: A new state of the water molecule. *Phys. Rev. Lett.*, 116:167802, 2016.

[21] Boris P. Gorshunov *et al.* Quantum behavior of water molecules confined to nanocavities in gemstones. *The Journal of Physical Chemistry Letters*, 4:2015–2020, 2013.

[22] M. Prencipe. Ab initio hartree–fock study and charge density analysis of beryl ($Al_4Be_6Si_{12}O_{36}$). *Phys Chem Min*, 29:552–561, 2002.

[23] Y. Finkelstein, R. Moreh, S. L. Shang, Y. Wang, and Z. K. Liu. Quantum behavior of water nano-confined in beryl. *The Journal of Chemical Physics*, 146:124307, 2017.

[24] Richard N. Zare. *Angular Momentum*. John Wiley & Sons, Inc., 1988.

[25] Dmitry Budker, Derek F. Kimball, and David P. DeMille. *Atomic physics: an exploration through problems and solutions*. Oxford University Press, 2012.

[26] J. M. Luttinger and L. Tisza. Theory of dipole interaction in crystals. *Physical Review*, 70:954–964, 1946.

[27] Pi Belobrov, Rs Gekht, and Va Ignatchenko. Ground-state in systems with dipole interactions. *Zhurnal Eksperimentalnoi I Teoreticheskoi Fiziki*, 84:1097–1108, 1983.

[28] B. P. Abolins, R. E. Zillich, and K. B. Whaley. Quantum phases of dipolar rotors on two-dimensional lattices. *J. Chem. Phys*, 148:102338, 2018.

[29] T. A. Kaplan and N. Menyuk. Spin ordering in three-dimensional crystals with strong competing exchange interactions. *Philosophical Magazine*, 87:3711–3785, 2007.

[30] Peter M. Felker, Vojtěch Vlček, Isaac Hietanen, Stephen Fitzgerald, Daniel Neuhauser, and Zlatko Bačić. Explaining the symmetry breaking observed in the endofullerenes $H_2@C_{60}$, $HF@C_{60}$, and $H_2O@C_{60}$. *Physical Chemistry Chemical Physics*, 19:31274–31283, 2017.

[31] Malcolm H. Levitt. Spectroscopy of light-molecule endofullerenes. *Philosophical Transactions of the Royal Society A: Mathematical, Physical and Engineering Sciences*, 371(1998):20120429, 2013.

[32] Jianying Sheng. Confined quantum molecular degrees of freedom. M.S. thesis, University of Waterloo, 2017.

[33] Yves Rubin. *Ring Opening Reactions of Fullerenes: Designed Approaches to Endohedral Metal Complexes*, pages 67–91. Springer Berlin Heidelberg, Berlin, Heidelberg, 1999.

[34] Z. Wang and C. Holm. Estimate of the cutoff errors in the Ewald summation for dipolar systems. *Journal of Chemical Physics*, 115:6351–6359, 2001.

[35] C. M. Soukoulis, K. Levin, and Gary S. Grest. Irreversibility and metastability in spin-glasses. i. ising model. *Phys. Rev. B*, 28:1495–1509, 1983.

[36] C. M. Soukoulis, G. S. Grest, and K. Levin. Irreversibility and metastability in spin-glasses. ii. heisenberg model. *Phys. Rev. B*, 28:1510–1523, 1983.

[37] Nicholas Wheeler. Higher-order spectral perturbation by a new determinantal method. (unpublished), Sept. 2000.

[38] Jens Jensen and Allan R Mackintosh. *Rare earth magnetism: structures and excitations*. Clarendon Press, 1991.

[39] Joseph V. Hajnal and Geoffrey I. Opat. Stark effect for a rigid symmetric top molecule: Exact solution. *Journal of Physics B: Atomic, Molecular and Optical Physics*, 24:2799–2805, 1991.

[40] Creighton K. Thomas and Helmut G. Katzgraber. Simplest model to study reentrance in physical systems. *Physical Review E - Statistical, Nonlinear, and Soft Matter Physics*, 84:1–4, 2011.

[41] Russell D. Johnson III. Nist computational chemistry comparison and benchmark database. NIST Standard Reference Database Number 101 Release 21, August 2020, available:http://cccbdb.nist.gov/NIST.

[42] T. Narayanan and Anil Kumar. Reentrant phase transitions in multicomponent liquid mixtures. *Physics Reports*, 249:135 – 218, 1994.

[43] R. Martonák, D. Marx, and P. Nielaba. Quantum fluctuations driven orientational disordering: A finite-size scaling study. *Phys. Rev. E*, 55:2184–2194, 1997.

[44] David C. Johnston. Magnetic dipole interactions in crystals. *Phys. Rev. B*, 93:014421, 2016.

[45] Hans-Joachim Werner, Frederick R. Manby, and Peter J. Knowles. Fast linear scaling second-order møller-plesset perturbation theory (mp2) using local and density fitting approximations. *J. Chem. Phys*, 118:8149, 2003.

[46] Satoru Kuwajima and Arieh Warshel. The extended ewald method: A general treatment of long-range electrostatic interactions in microscopic simulations. *The Journal of Chemical Physics*, 89:3751–3759, 1988.

[47] Salvatore Mamone, Mark R. Johnson, Jacques Ollivier, Stéphane Rols, Malcolm H. Levitt, and Anthony J. Horsewill. Symmetry-breaking in the $H_2@C_{60}$ endofullerene revealed by inelastic neutron scattering at low temperature. *Physical Chemistry Chemical Physics*, 18:1998–2005, 2016.

[48] S. W. de Leeuw, J. W. Perram, E. R. Smith, and John Shipley Rowlinson. Simulation of electrostatic systems in periodic boundary conditions. i. lattice sums and dielectric constants. *Proceedings of the Royal Society of London. A. Mathematical and Physical Sciences*, 373:27–56, 1980.

[49] Matthew Enjalran and Michel J. P. Gingras. Theory of paramagnetic scattering in highly frustrated magnets with long-range dipole-dipole interactions: The case of the $tb_2ti_2o_7$ pyrochlore antiferromagnet. *Phys. Rev. B*, 70:174426, 2004.

[50] S. N. Andreev, V. P. Makarov, V. I. Tikhonov, and A. A. Volkov. Ortho and Para Molecules of Water in Electric Field, 2014. arXiv:physics/0703038.

APPENDICES

Appendix A

Ewald summation

We want to calculate dipole-dipole interaction

$$\begin{aligned} H_{\text{Dipole}} &= \sum_{i>j} \frac{1}{4\pi\epsilon_0} \frac{\mathbf{d}_i \cdot \mathbf{d}_j - 3(\mathbf{d}_i \cdot \hat{\mathbf{r}}_{ij})(\mathbf{d}_j \cdot \hat{\mathbf{r}}_{ij})}{|\mathbf{r}_{ij}^3|}, \\ &= D \sum_{i>j} \Lambda_{ij}^{\alpha\beta} n_i^\alpha n_j^\beta, \end{aligned} \tag{A.1}$$

where

$$\Lambda_{ij}^{\alpha\beta} = -\partial_\alpha \partial_\beta \frac{1}{\mathbf{r}}, \tag{A.2}$$

is the coupling matrix for dipoles separated by a distance $\mathbf{r}$. To calculate an infinite lattice sum(the coupling matrix), we set periodic boundary conditions on a finite-sized system to unlimited range and write

$$\Lambda_{ij}^{\alpha\beta} = -\partial_\alpha \partial_\beta {\sum_{\mathbf{n}}}' \frac{1}{|\mathbf{r}_{ij} + \mathbf{n}|}, \tag{A.3}$$

where L is the linear size of the center box containing N dipoles in the direction of lattice translation vectors and $\mathbf{n}$ is a translation vector of the simulation box which contains the lattice. The prime on the summation sign means that sum does not include the $\mathbf{n}$ term for $i = j$.The Coulomb or dipolar potential is slowly decaying at large distances, so the direct summation converges slowly. Ewald replace the above sum summation into two rapidly

convergent sums: one performed in the direct (real) space and the other sum performed in the reciprocal space. We use the identity

$$\frac{1}{r} = \frac{2}{\sqrt{\pi}} \int_0^\infty \exp\{-t^2 r^2\} dt, \tag{A.4}$$

and split it into two parts

$$\frac{1}{r} = \frac{2}{\sqrt{\pi}} \int_0^\kappa \exp\{-t^2 r^2\} dt + \frac{\mathrm{erfc}(\kappa r)}{r}, \tag{A.5}$$

where erfc is the complimentary error function and κ is called the splitting parameter. The final expression of $\Lambda_{ij}^{\alpha\beta}$ then can be written as

$$\begin{aligned}\Lambda_{ij}^{\alpha\beta} =& {\sum_{\mathbf{n}}}' \delta_{\alpha\beta} B(\mathbf{r}_{ij}+\mathbf{n}) - C(\mathbf{r}_{ij}+\mathbf{n})(\mathbf{r}_{ij}+\mathbf{n})^\alpha (\mathbf{r}_{ij}+\mathbf{n})^\beta \\ &+ \frac{4\pi}{L^3} \sum_{\mathbf{K}\neq 0} \frac{K_\alpha K_\beta}{K^2} \exp\{-K^2/4\kappa^2\} \exp\{i\mathbf{K}\cdot\mathbf{r}_{ij}\} - \frac{2\kappa}{\sqrt{\pi}}\delta_{ij},\end{aligned} \tag{A.6}$$

where $\mathbf{K}$ is the reciprocal lattice translation vector and

$$\begin{aligned}B(r) &= \mathrm{erfc}(\kappa/r^3) + (2\kappa/\pi^{\frac{1}{2}}) \exp\{-\kappa^2/r^2\}/r^2, \\ B(r) &= 3\mathrm{erfc}(\kappa/r^5) + (2\kappa/\pi^{\frac{1}{2}})(2\kappa^2 + 3/r^2) \exp\{-\kappa^2/r^2\}/r^2.\end{aligned} \tag{A.7}$$

The rigorous mathematical proofs and detailed discussions can be found in Ref. [48]. The Fourier transform of the coupling strength, $\tilde{\Lambda}(q)$, for Bravais lattices is then

$$\tilde{\Lambda}(q) = \frac{1}{2} \sum_{\mathbf{n}} \Lambda(\mathbf{na}) \exp\{i\mathbf{q}\cdot\mathbf{na}\}, \tag{A.8}$$

where $\mathbf{a}$ is the lattice translation vector. The final expression can be written as

$$\begin{aligned}\tilde{\Lambda}(q) =& \sum_{\mathbf{n}} \delta_{\alpha\beta} B(\mathbf{r}) - C(\mathbf{r}) \mathbf{r}^\alpha \mathbf{r}^\beta \\ &+ \frac{4\pi}{L^3} \sum_{\mathbf{K}\neq 0} \frac{(\mathbf{q}-\mathbf{K})_\alpha (\mathbf{q}-\mathbf{K})_\beta}{(\mathbf{q}-\mathbf{K})^2} \exp\{-(\mathbf{q}-\mathbf{K})^2/4\kappa^2\} - \frac{2\kappa}{\sqrt{\pi}}\delta_{ij},\end{aligned} \tag{A.9}$$

where $\mathbf{r} = \mathbf{na}$. The more general expression for non-Bravais lattices can be found in Ref. [49].

Appendix B

Background information for quantum rotor basis

We briefly introduced the $|JKM\rangle$ basis set function in this section. The Hamiltonian for the rotational motion of a rigid body is given in Eq. (1.1). The energy levels of a rigid rotor are calculated by the Schrödinger equation

$$H_{\text{Rotation}}\Psi(\phi,\theta,\chi) = E\Psi(\phi,\theta,\chi). \tag{B.1}$$

Ψ is the wave function of molecule orientation and Euler angles (ϕ, θ and χ) define the orientation of the molecule in the body fixed frame relative to some non-rotating space-fixed frame. We first consider the symmetric rotor.

The Hamiltonian of a rigid symmetric top molecule ($\mathrm{I}_a = \mathrm{I}_b < \mathrm{I}_c$) is given by Eq. (3.31),

$$H_{\text{Rotation}}^{\text{symmetric}} = A\mathbf{J}^2 + (C-A)\mathbf{J}_z^2, \tag{B.2}$$

where $\mathbf{J}$ is the total angular momentum operator and $\mathbf{J}_z$ is the angular momentum operator about the symmetry axis of the molecule. In order to study the property of rigid rotor, the coordinate representation of $|JKM\rangle$ basis for symmetric top rotor needs to be introduced [24]

$$\langle JKM|\theta,\phi,\chi\rangle = \sqrt{\frac{2J+1}{8\pi^2}}D^J_{MK}(\theta,\phi,\chi). \tag{B.3}$$

where $D^J_{MK}(\theta,\phi,\chi)$ (the orientation angles θ, ϕ and χ are defined in Fig. B.1) is the Wigner-D matrix (the MK element of the rotation matrix, which represents the angular

momentum J [24, 39]), defined as

$$D^J_{MK}(\theta,\phi,\chi) = e^{-iM\phi} d^J_{MK}(\theta) e^{-iK\chi} \tag{B.4}$$

where $d^J_{MK}(\theta)$ is Wigner small d matrix. The $d^J_{MK}(\theta)$ is defined as [24]

$$\begin{aligned} d^J_{MK}(\theta) = & \sqrt{(J+M)!(J-M)!(J+M')!(J-M')!} \\ & \times \sum_{\nu} \frac{(-1)^{\nu}}{(J-M'-\nu)!(J+M-\nu)!(\nu+M'-M)!} \\ & \times [\cos\frac{\theta}{2}]^{2J+M-M'-2\nu} [-\sin\frac{\theta}{2}]^{M'-M+2\nu}, \end{aligned} \tag{B.5}$$

where ν is all positive integers.

$|JKM\rangle$ is the basis set functions for symmetric top rotor that satisfy [24]

$$\begin{aligned} \mathbf{J}^2 |JKM\rangle &= J(J+1) |JKM\rangle, \\ \mathbf{J}_Z |JKM\rangle &= M, \\ \mathbf{J}_z |JKM\rangle &= K. \end{aligned} \tag{B.6}$$

The quantum number K is for rotation about a symmetric axis in the principal axis system frame with $K\hbar$ as the projection of angular momentum onto the symmetric axis of the principal axis system frame. The quantum number M is for rotation about the Z-axis in the space-fixed frame with $M\hbar$ as the projection of angular momentum onto the Z-axis (see Fig. B.1). The energies for the symmetric rotor are

$$E(J,M) = AJ(J+1) + (C-A)K^2. \tag{B.7}$$

The linear rotor is the special case of the symmetric rotor, the moment of inertia for the symmetric axis is 0, and the rest two moment of inertia are equal. The symmetric top wave function $|J0M\rangle$ reduces to the spherical harmonic wave function $|JM\rangle$. For the asymmetric rotor case, the rotational energy can be written in the symmetric top basis, and the eigenvectors of the asymmetric top rotor are linear combinations of symmetric top wave functions. The rotational energy levels are labelled with J_{K_a,K_c}, $K_a, K_c = J, J-1, ..., 0$. The K_a is associated with a rotation about the a-axis and K_c, the c-axis. The symmetry about the b-axis can be obtained from the parity of the sum $K_a + K_c$ [24].

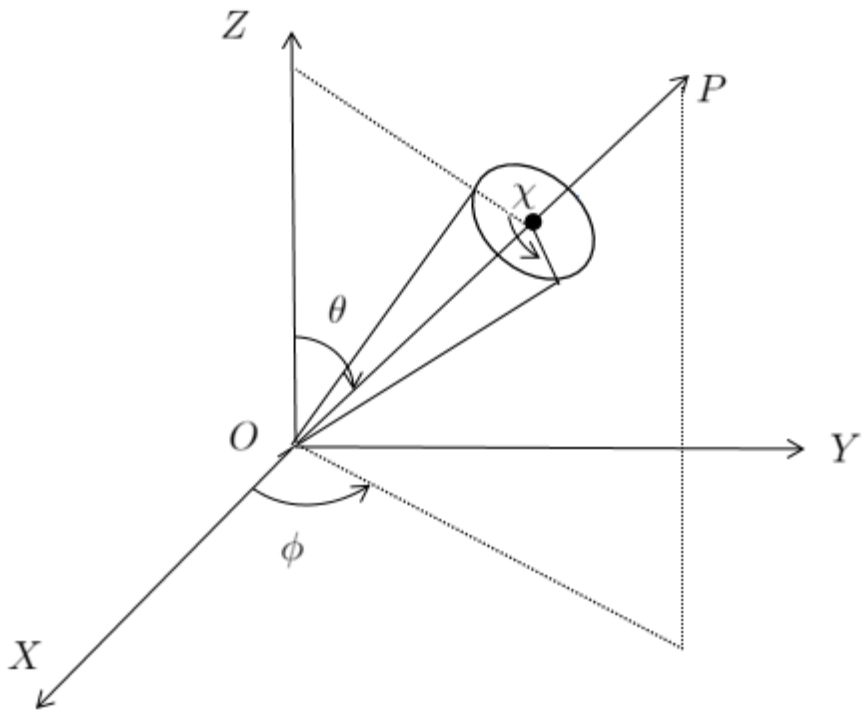

Figure B.1: Schematic view of the symmetric top rotor. The angles θ, ϕ (the spherical polar angles of the rotor axis) and χ (the angle of spin about the symmetric axis, i.e., OP) specify the ornentation of a symmetric top molecule.

Appendix C

Ortho and para water

Water molecules have two spin isomers, which are para water and ortho water. In order to reveal the fundamental properties and the interesting quantum phenomena of water molecules in the non-hydrogen bonding environments, the ortho-para spin conversion of the endofullerene $H_2O@C_{60}$ has been extensively studied [13, 16] (the ortho-para spin conversion of the water molecules have not been found in the INS spectra of beryl [13]). In this section, the background information for ortho and para water is given.

The rotational part Hamiltonian of water molecules ($I_a < I_b < I_c$) is given by

$$H_{\text{Rotation}} = A\mathbf{J}_a^2 + B\mathbf{J}_b^2 + C\mathbf{J}_c^2. \tag{C.1}$$

The symmetry of the Hamiltonian Eq. (C.1) belongs to the D_2 group, and the rotational energy levels belong to one of the symmetry species (A, B_a, B_b and B_c) of the D_2 group. After rotation by π along the b-axis (dipole moment of the water is along this axis) in the body frame ($C_\pi(b)$), the wave functions of the symmetry species A and B_b do not change their signs, while the B_a and B_c change their signs. In the Born-Oppenheimer approximation and ignoring the rotation-vibration coupling, the total wave function of the water can be written as

$$|\Phi\rangle = |\phi_{\text{n}}\rangle \cdot |\phi_{\text{el}}\rangle \cdot |\phi_{\text{vib}}\rangle \cdot |\phi_{\text{rot}}\rangle\,, \tag{C.2}$$

where $|\phi_{\text{n}}\rangle$, $|\phi_{\text{el}}\rangle$, $|\phi_{\text{vib}}\rangle$ and $|\phi_{\text{rot}}\rangle$ are the nuclei spin, electronic, vibrational and rotational wave functions. The vibrational and electronic wave functions are symmetric with respect to the permutation of the two hydrogen atoms. This permutation is equivalent to the $C_\pi(b)$ rotation. For the case of the parallel proton spins ($I = 1$), the exchange of the protons

does not reverse the sign of $|\Phi\rangle$. In this case, only $|\phi_{\text{rot}}\rangle$ is responsible for the sign inversion of the $|\Phi\rangle$ and $|\phi_{\text{rot}}\rangle$ of the ortho molecule has either B_a or B_c symmetries. For the case of the anti-parallel proton spins ($I = 0$), the exchange of the protons reverses the sign of $|\Phi\rangle$. In this case, $|\phi_{\text{rot}}\rangle$ of the para molecule has either A or B_b symmetries. In the J_{K_a,K_c} expression of the rotational wave function, the states with odd $K_a + K_c$ corresponds to B_a and B_c symmetries and are the wave functions for the ortho water; and even $K_a + K_c$ correspond to A and B_b symmetries and are para water [16, 50].

The rotational Hamiltonian in the symmetric top basis is diagonal in quantum number J and M, thus needs only be solved in K blocks which have size $2J+1$ by $2J+1$ for each J level (see Appendix B). As no matrix elements couple between odd and even K states, states correspond to odd, and even K blocks can be solved separately. The para states are from diagonalizing in the even K, while the ortho family is from diagonalizing in the odd K [24] (see Table 6.4 in Ref. [24]).